Swinging Atwood machine: experimental and numerical results, and a theoretical study

6 authors, including:

Olivier Pujol
Université de Lille
48 PUBLICATIONS   207 CITATIONS

SEE PROFILE

Ramis jean-pierre
Paul Sabatier University - Toulouse III
84 PUBLICATIONS   2,154 CITATIONS

SEE PROFILE

Sergi Simon
University of Portsmouth
10 PUBLICATIONS   131 CITATIONS

SEE PROFILE

Jacques-Arthur Weil
University of Limoges
66 PUBLICATIONS   832 CITATIONS

SEE PROFILE

Some of the authors of this publication are also working on these related projects:

Linearised Higher Variational Equations   View project

Microware radiometric profiling study   View project

Swinging Atwood Machine: Experimental and numerical results, and a theoretical study

O. Pujol [a,*], J.P. Pérez [b], J.P. Ramis [c], C. Simó [d], S. Simon [e], J.A. Weil [f]

[a] Université de Lille, UFR de Physique fondamentale, Laboratoire d'Optique Atmosphérique, 59655 Villeneuve d'Ascq cedex, France
[b] Université de Toulouse, Laboratoire d'Astrophysique Toulouse-Tarbes, CNRS, 14 avenue Édouard Belin, 31400 Toulouse, France
[c] Université de Toulouse, Laboratoire Émile Picard, 118 route de Narbonne 31062 Toulouse, France
[d] Universitat de Barcelona, Departament de Matemàtica Aplicada i Anàlisi, Gran Via de les Corts Catalanes, 585, 08007 Barcelona, Spain
[e] University of Portsmouth, Department of Mathematics, Lion Terrace, Portsmouth, Hampshire PO1 3HF, United Kingdom
[f] Université de Limoges, Département Mathématiques Informatique, XLIM - UMR CNRS n. 6172, 123 avenue Albert Thomas, 87060 Limoges cedex, France

ARTICLE INFO

ABSTRACT

A *Swinging Atwood Machine* (*SAM*) is built and some experimental results concerning its dynamic behaviour are presented. Experiments clearly show that pulleys play a role in the motion of the pendulum, since they can rotate and have non-negligible radii and masses. Equations of motion must therefore take into account the moment of inertia of the pulleys, as well as the winding of the rope around them. Their influence is compared to previous studies. A preliminary discussion of the role of dissipation is included. The theoretical behaviour of the system with pulleys is illustrated numerically, and the relevance of different parameters is highlighted. Finally, the integrability of the dynamic system is studied, the main result being that the machine with pulleys is non-integrable. The status of the results on integrability of the pulley-less machine is also recalled.

© 2010 Elsevier B.V. All rights reserved.

1. Introduction

This paper deals with the *Swinging Atwood Machine* (*SAM*), a non-linear two-degrees-of-freedom system derived from the well-known simple *Atwood machine*. The latter was devised in 1784 by George Atwood, a London Physics lecturer who built his own apparata as a means of practical illustration, in order to experimentally demonstrate the uniformly accelerated motion of a system falling under the local Earth gravity field g with mass dependence [1]. In Atwood original machine, two masses are mechanically linked by an inextensible thread wound round a pulley. In *SAM*, one of the masses (m) is allowed to swing in a plane while the other mass (M) plays the role of a counterweight; it is thus convenient to introduce the factor $\mu = M/m$ to study *SAM* dynamics.

For about twenty-five years, many studies have been conducted concerning the mechanical behaviour of *SAM*. Said studies were conducted exclusively on a simplified model for *SAM* neglecting any influence from a massive set of pulleys. Through numerical investigations, [2] inferred the pulley-less *SAM* to be an extremely intricate system exhibiting significant changes in the qualitative behaviour of trajectories, depending on μ-values. Assuming $\mu > 1$, motion is limited in space and two types of trajectories can be distinguished owing to the initial conditions: singular ones for which pendulum length is initially zero, and non-singular ones where the pendulum is initially released from rest with a non-zero length. For the former, it appears that $\mu = 3$ is a particular condition corresponding to terminating trajectories, i.e. those for which pendulum length becomes zero after a given duration [3]. The latter is divided into periodic, quasi-periodic and what can be conjectured to be ergodic trajectories in some domain. *SAM* without massive pulleys was also studied by means of Poincaré sections wherein chaotic dynamic behaviour becomes prominent as μ is increased [4]. An interesting and surprising result is the integrability of the pulley-less *SAM* for $\mu = 3$, a conclusion which is also supported using Hamilton–Jacobi theory [5] and Noether symmetries [6]. For $\mu > 3$, [7] proved that *SAM* without massive pulleys is not integrable, contrary to what was speculated by [4]. The belonging of $\mu = M/m$ to a special set of parameters $\{\mu_p : p \in \mathbb{Z}\}$ was established as a necessary condition

* Corresponding author.
E-mail addresses: olivier.pujol@loa.univ-lille1.fr (O. Pujol), perez@ast.obs-mip.fr (J.P. Pérez), ramis.jean-pierre@wanadoo.fr (J.P. Ramis), carles@maia.ub.es (C. Simó), Sergi.Simon@port.ac.uk (S. Simon), Jacques-Arthur.Weil@unilim.fr (J.A. Weil).

for integrability; this result was proven independently in [7–9], and is proven in Remark 7.1(2) of the present paper as well. Moreover, unbounded trajectories ($\mu \leq 1$) have been studied via energetic considerations [10]; [11] identified and classified all periodic trajectories in the pulley-less *SAM* for $\mu = 3$. Finally, a very recent result co-written by one of the authors of the present article [12] proved the non-integrability of this pulley-less model for *SAM* for the exceptional values $\{\mu_p : p \in \mathbb{Z}\}$; this had been an open problem, at least, since [7] explicitly tackled the issue for the first time. It is worth noting that all of these studies are theoretical, albeit for the most part strongly supported by massive numerical simulations.

In this paper, we intend to describe a useful physical construction of *SAM* in detail, as well as present further experimental and theoretical results. In addition, a theoretical premise is introduced which stands as a novelty all its own: to wit, as suggested by experiments, pulleys are no longer neglected, in order to take account of non-zero radii and rotation around their axes of revolution. When dealing with N-degree-of-freedom non-linear systems, the modern researcher's tendency to restrict adjectives such as "complex" to $N \gg 1$ should not divert us from the fact that even the dynamics of apparently elementary cases such as $N = 2$ are often very difficult to determine [13], and thus a source of interest in their own right. As shown in this paper, such is the case for *SAM*. A schematic representation of *SAM* is featured in Section 2 partly aimed at the derivation of the equations of motion with pulleys in Section 3. The constructed apparatus is then described in detail in Section 4, and some experimental results are presented in Section 5. A comparison with the theoretical model is performed in Section 6 through numerical simulations of the general equation of motion obtained in Section 3. Section 7 is devoted to proving the non-integrability for *SAM*. The rigorous proof shown therein is requisite to definitely establish the non-integrability of *SAM*, hence incumbent upon any proper completion of experimental and numerical results. Indeed, although for some systems non-integrability is somehow suggested by a thorough Poincaré section analysis, chaotic zone detection may require extremely careful numerics and will at times become laborious — we might call this *shy chaos*. Furthermore the lack of integrability of some systems cannot be discovered by looking at the real phase space. There exist non-integrable systems without any recurrent motion in the real phase space and such that chaos is confined away from the real domain. For an example, see [14]. Finally, Section 8 concludes with perspectives on further experiments and some comments on results concerning integrability of the pulley-less case.

[2] suggested a *SAM* physical demonstration model using a vertically mounted air table, and alleged a successful experimental demonstration of the system's motions. However, there is no experimental result in the aforementioned reference and its proposed model for *SAM* is ostensibly farther away from the theoretical system than the model described herein (cf. Section 2). To our present knowledge, detailed experimental studies of *SAM*, let alone comparisons of any such experiments with the theory, do not exist in the literature prior to our work.

Therefore, our work arguably completes the above theoretical and experimental research on *SAM*, and, at the same time, opens new problems and sets a starting point for further experimental and theoretical studies.

2. Schematic representation of *SAM*

SAM is represented by the system $\mathscr{S}$ sketched in Fig. 1 and consisting of: a pendulum, considered as a material point A of mass m; a counterweight, considered as a material point B of mass M; a thread of length L linking A and B; two pulleys $\mathscr{P}$ and $\mathscr{P}'$ of radius R, distant from one another by a predetermined distance D.
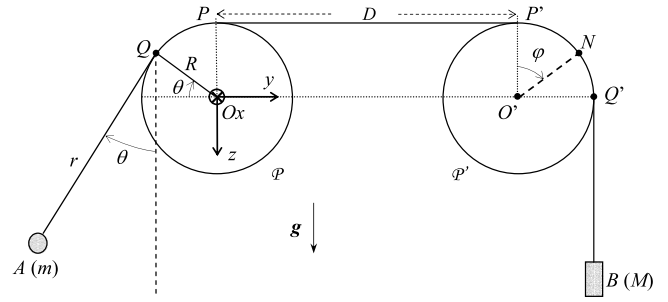

Fig. 1. Schematisation of the system $\mathscr{S} = \{$pendulum–thread–pulleys–counterweight$\}$ representing *SAM*. The angle φ locates the material point N of the pulley $\mathscr{P}'$.

$\mathscr{S}$ is studied relative to the Galilean laboratory frame $\mathscr{R} = (O\boldsymbol{e}_x\boldsymbol{e}_y\boldsymbol{e}_z)$ whose origin O is chosen to correspond to the centre of the pendulum pulley. Axis Ox corresponds to the pulley revolution axis; axis Oy is the horizontal direction defined by the pulley centres (O and O'), and oriented from O toward O'; finally, Oz is chosen to correspond, for the sake of convenience, to the downward direction of the vertical field $\boldsymbol{g}$.

Pendulum A is characterized by its variable length $r = QA$, Q being the geometrical point where the thread departs from the pulley, and by the angle θ formed by $\boldsymbol{QA}$ and the downward vertical. Note that θ as represented in Fig. 1 is a positive angle.

Vertical motion of the counterweight B is described by its coordinate z_B, which can be related to the angular position φ (positive angle) of any point N on the pulleys, provided the thread does not slip on the pulley (in Fig. 1, for the sake of clarity, N is drawn on the pulley $\mathscr{P}'$ associated to B). Indeed, under this assumption, when B is falling down, pulleys are able to rotate in such a way that the velocity of any point of the pulleys is equal to the velocity of B. Hence:

$$\dot{z}_B = R\dot{\varphi}. \tag{1}$$

Note the difference between the rotation angle φ of the pulleys and θ: the former defines the location of any material point on a pulley, whereas the latter defines the angular position of A, as well as that of the geometrical point of contact Q. This is due to the necessary mechanical description of contact in terms of three points [15]. A similar problem can be found in [16].

A physical way of understanding the difference between θ and φ is to imagine the following situation. At initial time, assume that Q and N are superposed: $\theta = \theta_0$ and $\varphi = \varphi_0$. If θ is fixed and B heads downwards with velocity $\dot{z}_B$, the absence of slippage of the thread on the pulleys implies that they rotate with angular velocity $\dot{\varphi}$ given by (1), meaning N is moving while Q remains fixed, and r evolves from r_0 to r; at final time, $\varphi \neq \varphi_0$.

Since L is supposed to be constant, z_B is directly related to r, D, and the lengths QP and $P'Q'$ corresponding to regions where the thread and the pulleys keep contact. Because

$$QP = R\left(\frac{\pi}{2} - \theta\right), \qquad P'Q' = \frac{\pi R}{2},$$

one has, precisely,

$$L = r + D + \pi R - R\theta + z_B. \tag{2}$$

Since $0 = \dot{r} - R\dot{\theta} + \dot{z}_B$, it follows that

$$\dot{\varphi} = \frac{\dot{z}_B}{R} = \frac{R\dot{\theta} - \dot{r}}{R}. \tag{3}$$

Hence, $\mathscr{S}$ is a system with two degrees of freedom, for instance θ and r.

3. Equations of motion of *SAM* with pulleys

3.1. Equations of motion

Let us determine the equations of motion for *SAM* by taking into account the pulleys, as opposed to what has been assumed in previous theoretical studies [2,4,5,10,6,3,11,8]. Indeed, their non-zero radii imply a likely change in position for Q, and $\mathcal{P}$ and $\mathcal{P}'$ are able to rotate around their respective revolution axes. Observations will confirm this — see Section 5.

Lagrangian formalism is used to derive these equations. The kinetic energy of the system is expressed by, with I_p the moment of inertia of one pulley:

$$\mathcal{E}_k = \frac{1}{2}mv_A^2 + \frac{1}{2}Mv_B^2 + 2\left(\frac{1}{2}I_p\dot{\varphi}^2\right).$$

The first term sums up the contribution by pendulum A, the second is relative to the counterweight B and the third one corresponds to the rotation of the two pulleys. We have:

$$\boldsymbol{v}_A = \frac{\mathrm{d}\boldsymbol{OA}}{\mathrm{d}t} = \frac{\mathrm{d}\boldsymbol{OQ}}{\mathrm{d}t} + \frac{\mathrm{d}\boldsymbol{QA}}{\mathrm{d}t},$$

where $\boldsymbol{OQ} = -R\cos\theta\boldsymbol{e}_y - R\sin\theta\boldsymbol{e}_z$ and $\boldsymbol{QA} = -r\sin\theta\boldsymbol{e}_y + r\cos\theta\boldsymbol{e}_z$, hence in the Cartesian base $(\boldsymbol{e}_x\boldsymbol{e}_y\boldsymbol{e}_z)$ we can write

$$\boldsymbol{v}_A = \begin{pmatrix} 0 \\ R\dot{\theta}\sin\theta - r\dot{\theta}\cos\theta - \dot{r}\sin\theta \\ -R\dot{\theta}\cos\theta - r\dot{\theta}\sin\theta + \dot{r}\cos\theta \end{pmatrix}.$$

Similarly, $\boldsymbol{v}_B = \mathrm{d}\boldsymbol{OB}/\mathrm{d}t$ with $\boldsymbol{OB} = z_B\boldsymbol{e}_z$. Using (2), one gets

$$\boldsymbol{v}_B = \dot{z}_B\boldsymbol{e}_z = \left(R\dot{\theta} - \dot{r}\right)\boldsymbol{e}_z.$$

Finally, using (3) and introducing the *effective total mass* of the system

$$M_t = M + m + \frac{2I_p}{R^2},$$

we get

$$\mathcal{E}_k = \frac{1}{2}M_t(R\dot{\theta} - \dot{r})^2 + \frac{1}{2}mr^2\dot{\theta}^2.$$

This expression is similar to that obtained when neglecting the pulleys, except that: the total mass is now different from $M + m$ by the term $2I_p/R^2$ conveying the rotation of the pulleys; the counterweight influences pendulum A through its length r and the winding of the rope on the associated pulley. The latter influence is considered in the term $R\dot{\theta}$.

Potential energy is only due to the Earth's local gravity field. Dropping an irrelevant additional constant term, we have:

$$\mathcal{E}_{p,g} = -m\boldsymbol{g}\cdot\boldsymbol{OA} - M\boldsymbol{g}\cdot\boldsymbol{OB} = -mgz_A - Mgz_B,$$

so that

$$\mathcal{E}_{p,g} = mg(R\sin\theta - r\cos\theta) + Mg(r - R\theta).$$

The Lagrangian $\mathcal{L}(r, \theta, \dot{r}, \dot{\theta}) = \mathcal{E}_k - \mathcal{E}_{p,g}$ of the system is thus:

$$\mathcal{L}(r, \theta, \dot{r}, \dot{\theta}) = \frac{1}{2}M_t(R\dot{\theta} - \dot{r})^2 + \frac{1}{2}mr^2\dot{\theta}^2 - gr(M - m\cos\theta) \\ - gR(m\sin\theta - M\theta).$$
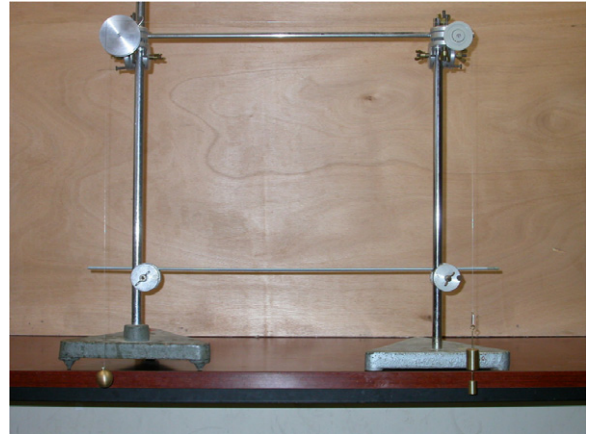
Equations of motion, without any dissipative term, follow from the Lagrange's equations:

$$\frac{\mathrm{d}}{\mathrm{d}t}\left(\frac{\partial\mathcal{L}}{\partial\dot{r}}\right) - \frac{\partial\mathcal{L}}{\partial r} = 0 \quad \text{and} \quad \frac{\mathrm{d}}{\mathrm{d}t}\left(\frac{\partial\mathcal{L}}{\partial\dot{\theta}}\right) - \frac{\partial\mathcal{L}}{\partial\theta} = 0$$

yielding

$$\begin{cases} \mu_t(\ddot{r} - R\ddot{\theta}) &= r\dot{\theta}^2 + g(\cos\theta - \mu) \\ r\ddot{\theta} &= -2\dot{r}\dot{\theta} + R\dot{\theta}^2 - g\sin\theta \end{cases} \quad (4)$$

with $\mu = M/m$ and $\mu_t = M_t/m = 1 + \mu + \left(2I_p/mR^2\right)$.

Fig. 2. Photo of the Swinging Atwood Machine (*SAM*): a pendulum (on the left) and a counterweight (on the right), linked together by a nylon thread.

3.2. Alternative methods to obtain equations of motion

Eqs. (4) can also been obtained using *SAM* Hamiltonian $\mathcal{H}(r, \theta, p_r, p_\theta)$, where p_r and p_θ are the conjugate momenta associated to r and θ respectively, i.e.:

$$p_r = \frac{\partial\mathcal{L}}{\partial\dot{r}} = -M_t(R\dot{\theta} - \dot{r})$$

$$p_\theta = \frac{\partial\mathcal{L}}{\partial\dot{\theta}} = M_tR(R\dot{\theta} - \dot{r}) + mr^2\dot{\theta} = -Rp_r + mr^2\dot{\theta}.$$

We have the following:

$$\mathcal{H}(r, \theta, p_r, p_\theta) = \frac{1}{2}\left[\frac{p_r^2}{M_t} + \frac{(p_\theta + Rp_r)^2}{mr^2}\right] \\ + gr(M - m\cos\theta) + gR(m\sin\theta - M\theta). \quad (5)$$

For the current *SAM* machine, Hamiltonian stands for mechanical energy: $\mathcal{H} = \mathcal{E}_k + \mathcal{E}_{p,g}$. Then, equations of motion (4) follow from Hamilton's equations:

$$\dot{p}_r = -\frac{\partial\mathcal{H}}{\partial r} \quad \text{and} \quad \dot{p}_\theta = -\frac{\partial\mathcal{H}}{\partial\theta}.$$

Another way to derive equations of motion (4) is first to apply the angular momentum theorem at the mobile point Q [15] and then using the conservation of mechanical energy.

3.3. Comparison with previous studies

Without any pulley influence, i.e. pulley moment of inertia $I_p = 0$ and pulley radius $R = 0$, we recover the equations obtained by [2]:

$$\begin{cases} (1 + \mu)\ddot{r} &= r\dot{\theta}^2 + g(\cos\theta - \mu) \\ r\ddot{\theta} &= -2\dot{r}\dot{\theta} - g\sin\theta. \end{cases} \quad (6)$$

Obviously, if there is no oscillatory motion ($\theta = 0$), the well-known simple Atwood machine [1] is recovered:

$$M_t\ddot{r} = g(m - M). \quad (7)$$

4. Description of the experimental apparatus

A physical prototype for *SAM* has been built using two identical pulleys, a nylon thread, a brass ball as a pendulum and a set of different hook masses acting as counterweights. The pendulum and the chosen counterweight are linked together by the nylon thread placed around the pulleys. A photo of *SAM* is displayed in Fig. 2.
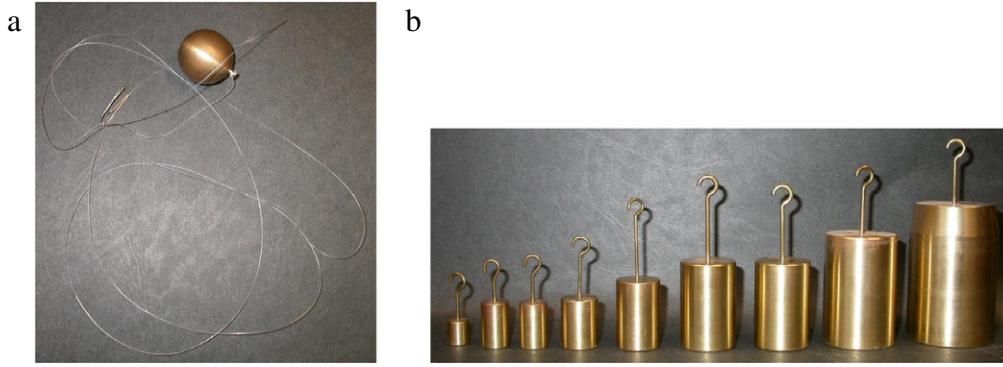
Fig. 3. (a) Brass ball (pendulum), nylon thread and paper clip (b) Set of hook masses used in the experiment (counterweight). From left to right: 10 g, 20 g, 20 g, 50 g, 100 g, 200 g, 200 g, 500 g, 1000 g.

4.1. About the pendulum and the counterweight

Each mass in the experimental device has been measured with a precision scale of 0.01 g of accuracy. The pendulum is a brass ball with a 30 mm diameter and a mass $m = 118.36$ g. The picture of the pendulum in Fig. 3(a) also exhibits a paper clip and the nylon thread, the latter being solidly tied to the brass ball and the paper clip.

The paper clip is secured to the hook of the chosen counterweight, in turn picked out from nine hook masses whose measured values are $M = 10.01$ g, 20.02 g ($\times 2$), 50.05 g, 100.10 g, 200.22 g ($\times 2$), 500.51 g, and 1000.10 g (Fig. 3(b)). The relative difference between these values and those engraved in each hook mass is 0.1%; thus, with respect to the orders of magnitude of the different masses involved in the experimental device, this difference can be neglected. The values considered are therefore presumed to be those indicated on the hook mass themselves, namely $M = 10$ g, 20 g ($\times 2$), 50 g, 100 g, 200 g ($\times 2$), 500, and 1000 g. Henceforth, and for the sake of linguistic simplicity, these hook masses will be called "counterweights", although *weight* and *mass* are different notions, however related. This set enables varying the counterweight mass from 10 g (one mass) to 2100 g (addition of all the masses) with a step of 10 g by hooking several masses together. Among these hook masses, one is hung on the nylon thread by means of the paper clip, whose measured mass is 0.37 g. It is interesting to note that, by a fortunate coincidence, the mass of the paper clip is equal, with a 0.01 g difference, to 0.36 g, i.e. the mass of the brass ball minus 118 g. Therefore, with a good approximation, the mass of the brass ball can be taken as equal to 118 g and the mass of the paper clip can be ignored. Finally, we get, for the pendulum and the counterweight, respectively: $m = 118$ g and $10 \text{ g} \leq M \leq 2100$ g.

4.2. About the nylon thread and the pulleys

The thread (Fig. 3(a)) ensures a mechanical coupling between the pendulum and the counterweight through the two pulleys. The length of the thread is about one meter and its measured mass of 0.10 g is negligible compared to the other masses involved. In addition, the nylon thread is assumed inextensible. During experimentation, no thread breaking has been reported.

Pulleys used are shown in photos of Fig. 4. They are made up of two parts: an internal, immobile one bound to the revolution axis, and a mobile, external one liable to rotate around this axis. These two pulley components are uncoupled by means of a ball bearing which, moreover, reduces mechanical energy dissipation by friction. Pulley radius is $R = 2.5$ cm and that of the motionless part is 1 cm. Pulley $\mathcal{P}$, associated to the pendulum, has been modified in order to make its groove deeper. Indeed, during the

first experimentations we observed that the thread could rapidly exit the groove because of the pendulum motion. To avoid this, which could by the way be dangerous, two metallic plates were added and fixed to the pulley in order to increase by 1 cm the depth of the groove (Figs. 4(a) and (b)). It is worth noting that the plates are fixed to the immobile part of the pulley and are in no way in contact with the mobile one. The motion of the latter one is thus not affected by such a modification: hence, from a mechanical point of view, the resulting pulley is identical to the original one.

4.3. Strengthening of the apparatus

Fig. 2 also features two horizontal metallic rods binding the two feet of *SAM*. Their role is to reinforce the machine. Indeed, due to considerable stress involved in the pendulum and counterweight motions, the orientation of the two pulleys, as well as the arbitrary distance $D = 57.5$ cm between them, can change; thus, it could be dangerous not to strengthen the whole device. The lower metallic rod is solidly fixed to the feet while the upper one is solidly fixed to the revolution axes of the pulleys. Consequently, we ensured a constant distance between the pulleys whose axes keep a constant direction; in virtue of such a construction, *SAM* is solid and operational.

5. Motion of the pendulum: Experimental results

5.1. Experimental measure of I_p

The presence of the moment of inertia I_p of a pulley in (4) renders an experimental determination thereof necessary. This measure was made using a simple Atwood machine with only one pulley. The heavier mass ($M = 130$ g) fell down from a convenient height $h = 1.656$ m; the lighter mass (the brass ball) being $m = 118$ g. Using Eq. (7), one gets for the moment of inertia of a pulley:

$$I_p = R^2 \left[\frac{(M - m)g(\Delta t)^2}{2h} - (M + m) \right]$$

where Δt is the fall duration. Through a set of ten measures with a 0.01 s-accuracy chronometer, the mean fall duration found is $\langle \Delta t \rangle = 2.70 \pm 0.01$ s. In addition, the value of g used is 9.8043 m s^{-2}; it has been measured in Toulouse (France), precisely the site of the experiments [17]. $\langle I_p \rangle = 6.85 \times 10^{-6}$ kg m^2 ensues. Concerning the value of I_p, errors are due to the measure of both Δt and the positions of M at the initial and final times − that is, the determination of h. Uncertainties are mainly due to the determination of the final time, which must correspond to the falling distance h as precisely as possible; initial and final positions are determined with an error of 0.1 cm, which compared to the value of h can be neglected. Consequently, uncertainties in position
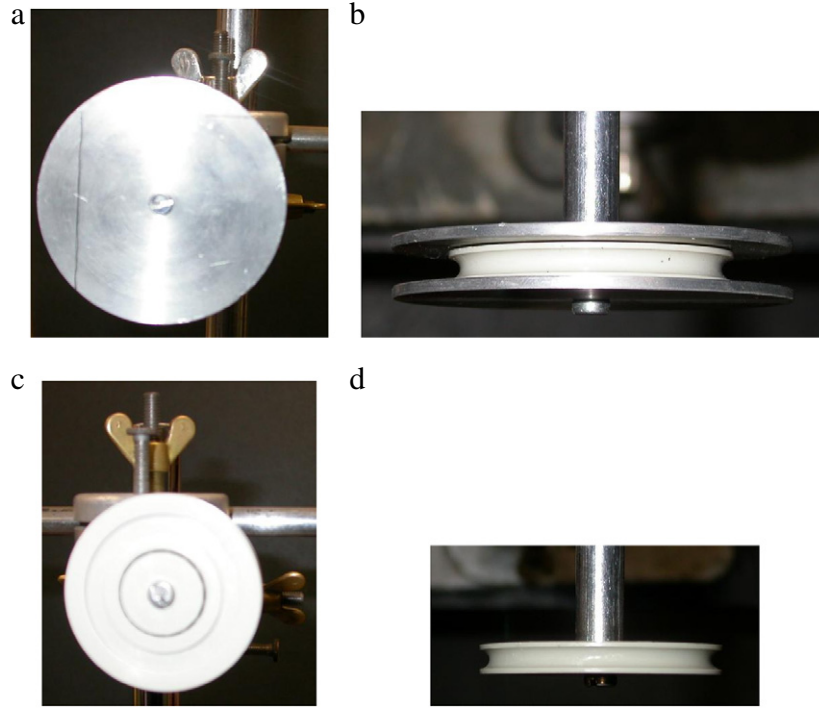
Fig. 4. Photos of the two pulleys. (a) Pulley $\mathcal{P}$, front view: a metallic plate is added which hides the internal part and the ball bearing of the original pulley. (b) Pulley $\mathcal{P}$, top view: the groove is made deeper by 1 cm with the additional plate; the original pulley is easily recognizable between the two plates. (c) Pulley $\mathcal{P}'$, front view: the ball bearing uncouples the immobile internal part and the mobile external one (d) Pulley $\mathcal{P}'$, top view: photograph of the axis of revolution and the groove of the pulley. Moreover, the two pulleys are distant enough from one another to avoid a pendulum–counterweight collision during the motion.

determinations are disregarded and the error in the measure of I_p can be reasonably associated to the uncertainty in Δt (0.4%). Thus, precision on I_p is twice that of Δt, hence about 1%; absolute uncertainty is thus 0.07×10^{-6} kg m². Therefore, we can write:

$$I_p = (6.85 \pm 0.07) \times 10^{-6} \text{ kg m}^2 \quad \text{or}$$

$$I_p = 6.85 \times 10^{-6} \text{ kg m}^2 \pm 1\%.$$

Another method to determine the moment of inertia of one pulley is to use an accelerometer to measure the acceleration of the heavier mass. The approach consists in loading the apparatus with the total constant mass $M + m$, and to make at least 8 different measurements of the acceleration by displacing a mass from one side of the pulley to the other, while keeping the total inertia constant. Plotting acceleration versus the difference $M - m$ and calculating the associated slope s, I_p is obtained by:

$$I_p = \frac{R^2}{2}\left[\frac{g}{s} - (M + m)\right].$$

5.2. Experimental results

The motion of the pendulum has been filmed for various μ-values and initial conditions $(r_0; \theta_0)$. Then, using the "Synchronie" software and focusing on each film image by image, a pointer enabled us to pick up pendulum positions and record them. Such a process is necessarily a source of errors, as it is sometimes difficult to locate the pendulum exactly, especially if velocity is high. The errors introduced by such a procedure are not simple to estimate. However, trajectories have been correctly recorded, as comparisons with numerical simulations of the theoretical equations will show (see Section 6). It must be pointed out that data acquisition has been stopped when, during the motion, the string appeared suddenly, and visibly, non-tensioned. Obviously, an appropriate sensor to determine string tension would be useful; that will be one of the features of a further paper.

5.2.1. Case $\mu_{\text{theo}} = 3$

Since previous studies focused mainly on the particular and theoretical case $\mu_{\text{theo}} = 3$, this was the first one we experimentally addressed. In fact, the masses available only allowed us to *approach* μ_{theo}: with $m = 118$ g and $M = 350$ g one obtains $\mu_{\text{exp}} = 2.966$, which is the closest value to μ_{theo}. The sampling time step has been 67 ms. Motion has been researched for four different initial conditions $(r_0; \theta_0) = (0.649; 53.5)$, $(0.710; 66.5)$, $(0.854; 68.3)$ and $(0.867; 51.1)$; r_0 is in meters, θ_0 in degrees. The corresponding films can be watched at the website http://www-loa.univ-lille1.fr/~pujol/. The motion of the pendulum presents the same pattern and characteristics for all these conditions, so only the trajectory for the first initial conditions is shown in Fig. 5(a). All in all, 359 sampling times have been recorded. The pendulum has a planar revolving trajectory around the pulley and presents an asymmetry with respect to the vertical direction. Note that the pendulum becomes closer and closer to the pulley as a consequence of dissipative phenomena and is bound to end up knocking against it. Phenomena qualifying as dissipative are, to our knowledge: the friction between the thread and the pulley, the air friction on the pendulum and the counterweight as well as friction inside the ball bearing. Evolutions of the length of the pendulum r and angle θ are displayed in Fig. 5(b) and (c) respectively. The asymmetry of the trajectory and dissipation are observable in the evolution of r since this variable exhibits different minimal and maximal amplitudes which decrease in function of time t.

The Fourier analysis (non-displayed) of the data shows that, for the behaviour of θ, the most relevant harmonic is the constant term, followed by harmonics 7, 6 and 8. They account, respectively, for 0.401, 0.311, 0.117, and 0.091 of the total variation. Of course, the contributions of harmonics 6 and 8 are due to leakage of the 7th one. The amplitude of the 6th harmonic is larger than that of the 8th, showing that the true dominant average frequency is slightly less than 7 times the basic frequency. From the number of data and the sampling step time, a basic frequency of 0.042 Hz

follows. Hence, an average value of the dominant frequency can be estimated to be equal to 0.294 Hz. However, as is clear by looking at the maxima of the angle, the frequency changes with time. The spacing between successive maxima takes the approximate values 3.820 s, 3.909 s, 3.379 s, 3.311 s, 3.173 s, 2.780 s, and 2.643 s. Hence, the instantaneous frequency changes from about 0.262 Hz to about 0.378 Hz. The explanation is simple: the dissipation reduces the energy and the length of the pendulum becomes shorter, increasing the frequency.

For the radius, the major contribution comes from the constant term, followed by harmonics 13 and 7. They account for 0.810, 0.037, and 0.026 of the total variation. Comparing the plot of r as a function of time with that of θ, one can see a doubling in the number of maxima. The explanation is simple: largest maxima occur at the left part of the plot of the orbit. Then, a minimum is reached when $\theta = -\pi$ (i.e., upwards), followed by a maximum to the right, and a new minimum at $\theta = -\pi$ to reach a larger maximum on the left. The spacing between successive larger maxima of r is very close to the one observed for θ. As mentioned, the largest non-constant harmonics are the 13th and the 7th, not in a 2-to-1 ratio. This is related to the fact that the "best" estimate of the main frequency for θ is slightly less than 7 times the basic frequency. The closest integer to the double would be 13 rather than 14.

The decrease in energy can be calculated as follows. From the experimental data, the values of $\dot{r}$ and $\dot{\theta}$ can be computed. For that, we have used two independent methods. The first one is simply numerical differentiation with a central formula. The second one aims at filtering errors in the data as well. A Discrete Fourier Transform has been computed and harmonics up to order 32 have been retained. Then, it is possible to check that the reconstruction agrees quite well with the initial data and one can compute the values of $\dot{r}$ and $\dot{\theta}$ using these Fourier expansions. To prevent leakage due to the fact that the data at the ends of the interval are quite different (Figs. 5(b) and (c)), which originates the well-known $O(1/n)$ decrease of the order of magnitude of the nth harmonic, different procedures have been used, but the results are essentially the same. They also show a reasonable agreement using the first and second methods.

When $\dot{r}$ and $\dot{\theta}$ are available, one can compute p_r and p_θ and subsequently the value of the energy. The values for which θ reaches a maximum (i.e., on the left of Fig. 5(a)) are shown in Fig. 6. The rate of decrease of the energy is about 0.037 J s^{-1}.

### 5.2.2. Case $\mu_{theo} = 1.5$

The experimental value of μ closest to $\mu_{theo} = 1.5$ is $\mu_{exp} = 1.525$, given by $M = 180$ g. Proceeding as in the above case allows us to retrieve the experimental trajectory and the evolution of the degrees of freedom. In this case, time step is 40 ms. Two initial conditions have been considered: $(r_0; \theta_0) = (0.484 \text{ m}; 87.0°)$ and $(0.621 \text{ m}; 87.7°)$. Since they produce the same dynamic behaviour, only the first one is displayed (Fig. 7(a), (b) and (c) respectively). The two films can be viewed on http://www-loa.univ-lille1.fr/~pujol/. A slight asymmetric trajectory with respect to the vertical direction and an evolution of θ close to periodic with a period around 1.1–1.2 s can be observed. For the evolution of r, asymmetry and slight dissipation are also observed.

A study similar to that of $\mu_{exp} = 2.966$ is performed. The main contribution to the Fourier analysis of θ comes from harmonic number 7 which accounts for 0.912 of the total variation with a frequency of approximately 0.875 Hz, although a better value for the average frequency seems to be 0.89 Hz. Harmonics 14 and 21 also play a relevant role. As we did for $\mu_{exp} = 2.966$, we can consider the spacing between successive maxima of θ which takes the values 1.125 s, 1.119 s, 1.114 s, 1.110 s, 1.156 s, 1.133 s and 1.063 s, showing a decreasing trend with irregularities.
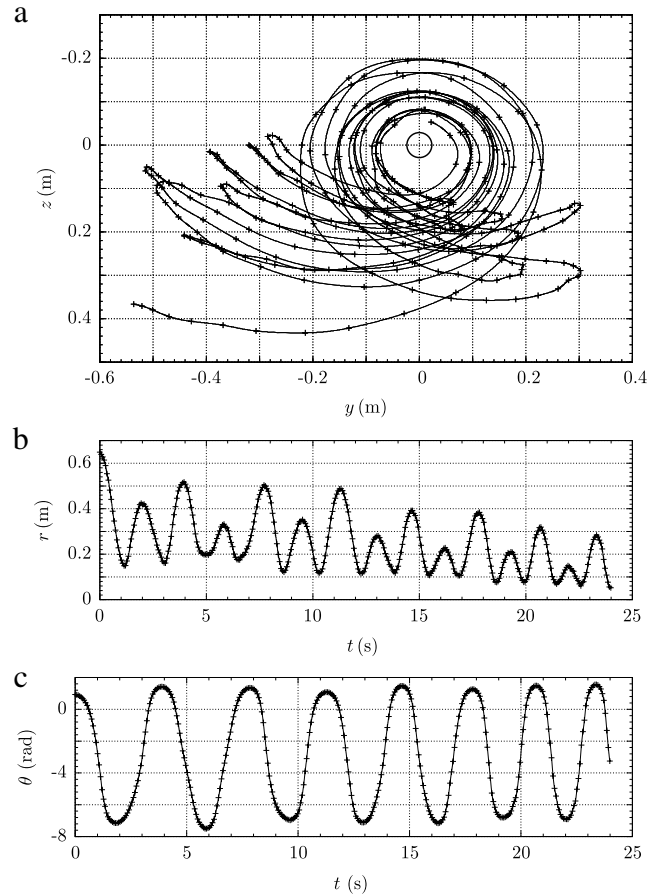

Fig. 5. Case $\mu_{exp} = 2.966$ with initial conditions $r_0 = 0.649$ m and $\theta_0 = 53.5°$. (a) Experimental positions (black crosses) and interpolated pendulum trajectory (solid line). The Cartesian coordinates of the initial position are $y = -0.54$ m and $z = 0.37$ m and those of the final position are $y = 0.02$ m and $z = -0.05$ m. The pulley is represented by the circle whose centre is at the origin of coordinates (0; 0). (b) Experimental positions (black crosses) and interpolated curve (solid line) for the evolution of r. (c) Same as (b) but for the angle θ.
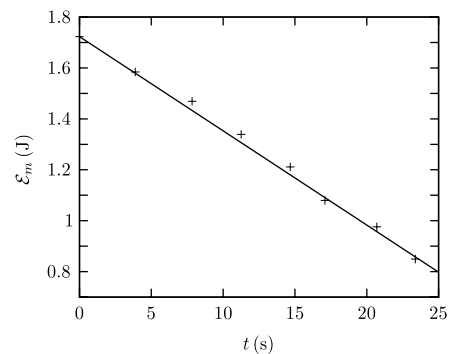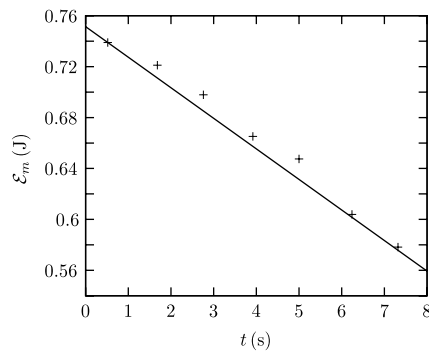

Fig. 6. Values of the energy (crosses) occurring when θ reaches a maximum at the left part of Fig. 5(a). We have also displayed the function $\mathcal{E}_m = 1.723 - 0.037t$.

For r, the largest harmonic is the constant term which accounts for 0.971 of the signal. If we skip this term, harmonics 7, 14 and 3 are clearly seen. They contribute to 0.30, 0.29, and 0.14 of the signal minus the constant part.

The decrease of the energy as a function of time has been displayed in Fig. 8, this time using the values of the energy computed at the minima of θ, on the right part of Fig. 7(a). Now the rate of decrease is about 0.024 J s^{-1}. In this case, using the filtered Fourier methods gives better results, because of the large changes in position with a time step of 40 ms.
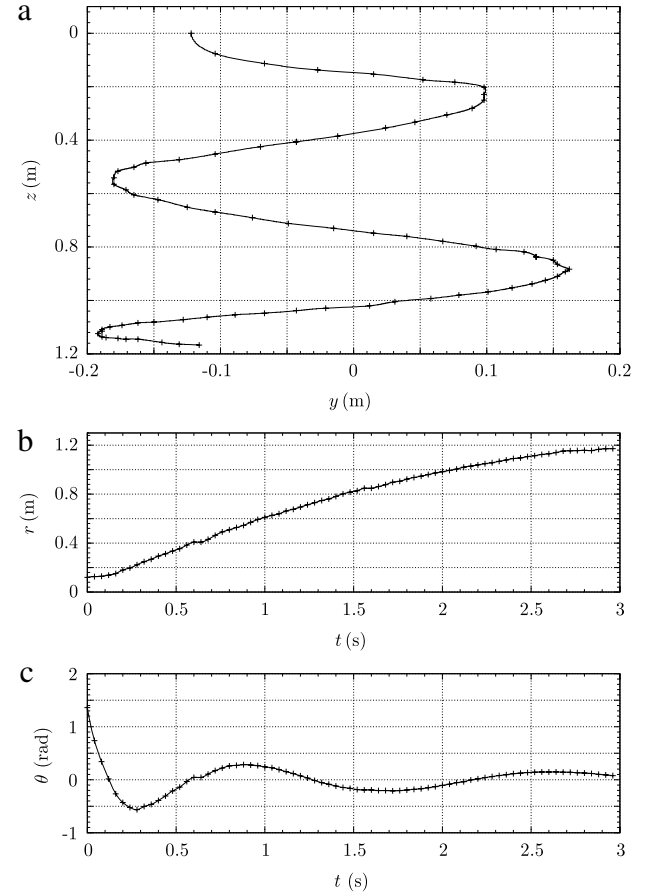
a

b

c
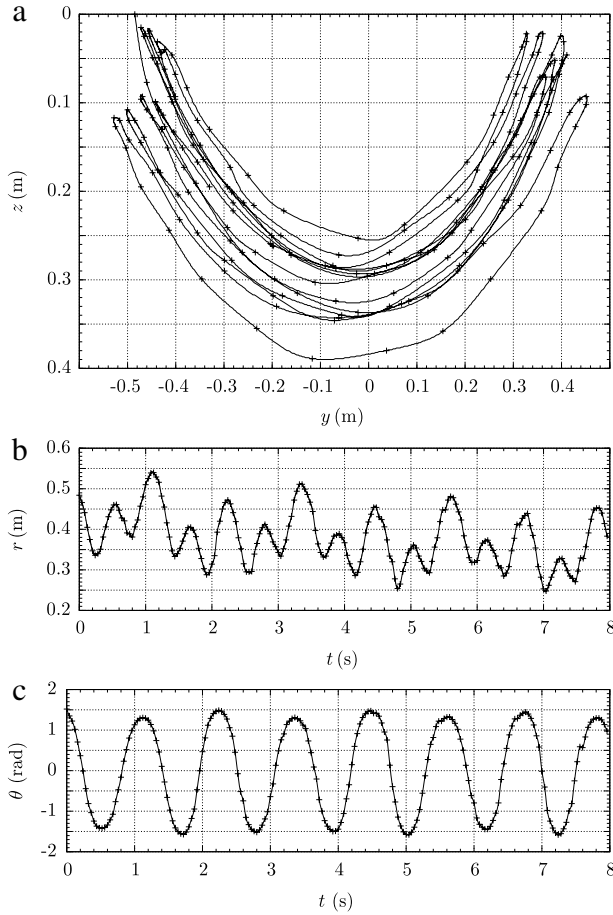
Fig. 7. Same as Fig. 5 but for $\mu_{\exp} = 1.525$ and initial conditions $r_0 = 0.484$ m and $\theta_0 = 87.0°$. In (a), the Cartesian coordinates of the initial position are $y = -0.485$ m and $z = 0$; for the final position, one has $y = -0.330$ m and $z = 0.195$ m. The origin $(0; 0)$ corresponds to the centre of the pulley (not represented).

Fig. 8. Values of the energy (crosses) occurring when θ reaches a minimum at the right part of Fig. 7(a). We have also displayed the function $\mathcal{E}_m = 0.751 - 0.024t$.

5.2.3. An unbounded case: $\mu_{\text{theo}} = 1$

In this situation, the experimental value of μ is $\mu_{\exp} = 1.017$ and three initial conditions have been considered: $r_0 = 0.120$ m, 0.263 m and 0.477 m for $\theta_0 = 77.9°$. Again, trajectories present the same pattern, so only one is shown (Fig. 9(a)). The films are available on http://www-loa.univ-lille1.fr/~pujol/. They are characterized by an increase in r and θ oscillations around the vertical ($\theta = 0$) with a decreasing amplitude of θ (Fig. 9(b) and (c)) respectively). In Fig. 9(b), r appears to approach a linear increase in time: $r = v_z t$ where v_z is the velocity along the vertical.

a

b

c

Fig. 9. Same as Fig. 5 but for $\mu_{\exp} = 1.017$ and initial conditions $r_0 = 0.120$ m and $\theta_0 = 77.9°$. In (a), the Cartesian coordinates of the initial position are $y = -0.122$ m and $z = 0$; for the final position, one has $y = -0.116$ m and $z = 1.167$ m. The origin $(0; 0)$ corresponds to the centre of the pulley (not represented).

6. Numerical solution of *SAM* equations of motion

6.1. Theoretical trajectories

Equations of motion (4) have been numerically integrated for the same initial conditions and values of the parameter μ as above in order to compare the theoretical trajectories, displayed in Fig. 10, with the experimental ones. Computation of the theoretical trajectories has been performed by using both a Taylor integration method and a variety of Runge–Kutta methods of different orders with step-size control to integrate the equations of motion.

From a general point of view, the theoretical trajectories seem quite similar to the experimental ones. However, some slight differences can be detected. Firstly, it is obvious that dissipative phenomena, albeit experimentally reduced, play a non-negligible role since convergence of the pendulum towards the pulley for the first case (Fig. 5(b)), decrease of r for the second one (Fig. 7(b)) and relatively slow increasing of r for the third one (Fig. 9(b)) are clearly associated to energy dissipation. Friction will be studied a bit further in Section 6.4 and much more in future works. Secondly, for $\mu_{\exp} = 2.966$, it has been observed that the mass m touches the horizontal nylon thread between the two pulleys when it revolves around the Ox axis (Fig. 1). This influence of the thread could be included into the equations of motion through a dissipative term, although it seems quite difficult to introduce such an effect in a realistic manner.

An important point concerns the comparison between these trajectories and those of [2]. For the first case for instance, the

Tufillaro trajectories are symmetrical with respect to the vertical direction, as opposed to the above ones (Figs. 5(a) and 10(a)). Clearly, this asymmetry is due to the influence of the pulleys.

6.2. Influence of the pulleys on the motion

Pulleys can influence the motion of *SAM* through their dimension (since radius $R \neq 0$) and their rotation (since $I_p \neq 0$).

6.2.1. Influence of the radius: $\mu_{exp} = 2.966$

Fig. 11 sketches the trajectory for $\mu_{exp} = 2.966$ when $I_p = 0$ for different values of increasing R; i.e. the pendulum pulley $\mathcal{P}$ has a non-negligible radius but pulleys are not allowed to rotate. The first figure corresponds to the symmetrical Tufillaro trajectory ($R = 0, I_p = 0$). Ostensibly, the larger R is, the more significant the asymmetry becomes. For $R = 5$ cm, and for the initial conditions chosen, the pendulum hits the pulley before completing one revolution; obviously, with an initial length of the thread more important, the pendulum do not hit the pulley.

6.2.2. Influence of the moment of inertia: $\mu_{exp} = 2.966$

Fig. 12 sketches the trajectory for $\mu_{exp} = 2.966$ for increasing values of I_p with a value of pulleys radius taken to the real value $R = 2.5$ cm. The trajectory of the pendulum is visibly modified: it describes more irregular trajectories and fills more space as I_p increases.

6.2.3. Influence of the pulleys: $\mu_{exp} = 1.525$

In this case, results of variations in R with $I_p = 0$ (Fig. 13) and I_p variations for $R = 2.5$ cm (Fig. 14) are similar in that trajectories are modified more visibly as R and I_p increase. However, the influence of I_p and R on *SAM* motion depends on the value of μ considered. If R increases, the pulleys being fixed, the brass ball ends up hitting the pulley but asymmetry does not becomes more and more important. If I_p increases, pulley dimensions being fixed, the pendulum evolves in a much more limited space.

6.3. Poincaré maps and rotation number

To have a global view of the dynamics of *SAM*, we have computed Poincaré maps $\mathcal{P}_m$ on suitable Poincaré sections. We note that the Hamiltonian (5) is not 2π-periodic because of the linear term in θ. Be that as it may, our Poincaré section Σ defining $\mathcal{P}_m$ is given by the coiling of θ through multiples of 2π, with $\dot{\theta} > 0$. But, contrarily to *SAM* without pulleys [4], one has to distinguish between cuts through different multiples of 2π. Plus, one cannot superimpose the different sheets.

Some types of "escape" can occur. The main source thereof is r going to zero. Other relevant sources of escape are r increasing too much or $|\theta|$ becoming too large. All orbits leading to some of these escapes are deleted.

To compare with the experiments, we present some examples for $M = 350$ g and $M = 180$ g. As levels of energy, one has taken the values corresponding to the experiments described in 5.2.1 and 5.2.2, that is, $(r_0; \theta_0) = (0.649$ m; $53.5°)$ and $(r_0; \theta_0) = (0.484$ m; $87.0°)$, respectively, with zero initial velocity. Given r, p_r in Σ and $\theta = 0$, the value of p_θ is recovered from the energy level. Fig. 15 shows some results. All these massive computations use Taylor integration methods, in order to ensure a very good conservation of the energy (see, e.g., [18]).

The top left plot corresponds to $M = 350$ g, leaving Σ with $p_r > 0$. The points on Σ with $p_r < 0$ correspond to cuts through $\theta = -2\pi$, in agreement with the description of motion in 5.2.1. To produce the Poincaré map, we first computed the periodic orbit as a fixed point in $\Sigma \cap \{p_r > 0\}$. The approximate values $(r^*; p_r^*)$
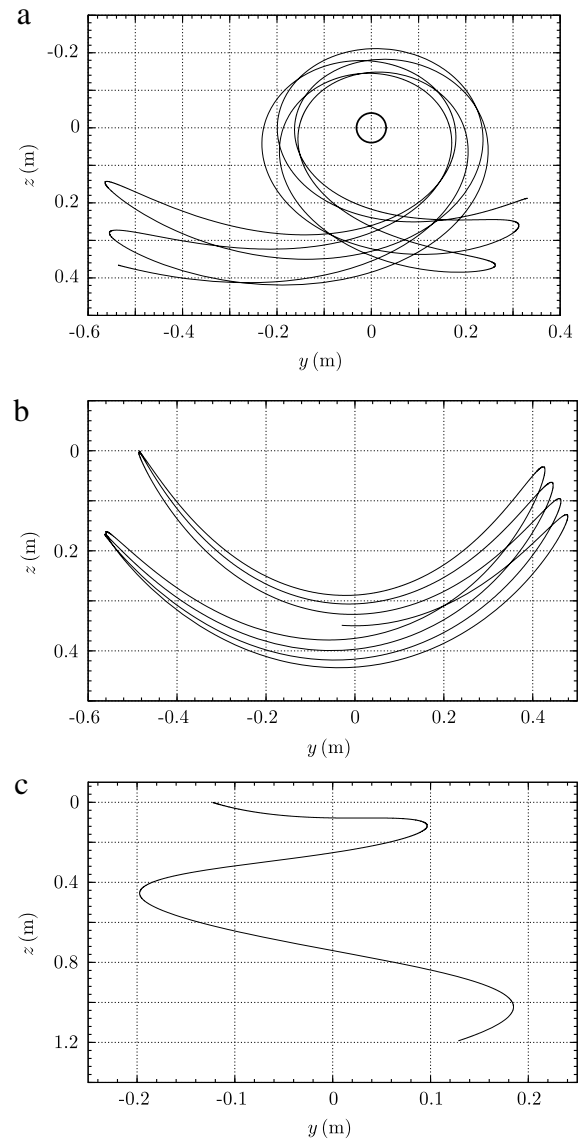

Fig. 10. Numerical trajectories obtained by solving equations of motion (4). (a) $\mu_{exp} = 2.966$ and for the same initial conditions as Fig. 5(a). (b) $\mu_{exp} = 1.525$ and for the same initial conditions as Fig. 7(a). (c) $\mu_{exp} = 1.017$ and for the same initial conditions as Fig. 9(a).

of the fixed point are (0.332814 m; 0.554330 kg m s⁻¹). This periodic orbit can also be obtained by starting the motion from rest at $(r_0; \theta_0) \approx (0.61316$ m; $64.032°)$, not too far from the values used in the experiment. The curve drawn with large dots around the periodic orbit shows the iterates of $\mathcal{P}_m$ corresponding to the data used in the experiment. It is clear that the theoretical, non-dissipative, motion seems to be in a 2D torus, but numerical computations can never exclude the possibility of having a periodic orbit with very long period or a tiny chaotic zone. The intersection of this torus with $\theta = -2\pi$ is also shown in the region $p_r < 0$. The asymmetry is ostensible in the plot, and is due to the effect of the pulleys. To produce the full plot, we have taken initial conditions on Σ with $r = r^*$ and different values of p_r starting at p_r^*. From some value of p_r onwards, iterates escape. We do not exclude the presence of tiny islands outside the last invariant curve shown.

For the sake of completeness, we show in the top right plot the Poincaré iterates leaving Σ in the region $\{p_r < 0\}$. Points appearing in $\{p_r > 0\}$ are on the sheet $\{\theta = 2\pi\}$. The fixed point in $\{p_r < 0\}$ is approximately (0.383367 m; −0.620020 kg m s⁻¹).
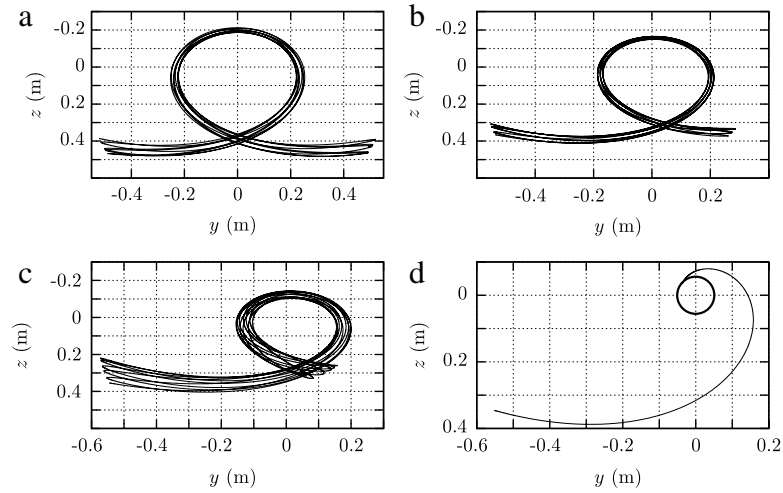
Fig. 11. Theoretical trajectories of the pendulum with fixed pulleys of different radii R for $\mu_{exp} = 2.966$ and initial condition $(r_0; \theta_0) = (0.649 \text{ m}; 53.5°)$. (a) $R = 0$, (b) $R = 2.5$ cm, (c) $R = 4$ cm and (d) $R = 5$ cm. In the latter subplot, the pulley has been represented by the circle whose centre is at the origin of coordinates in order to see the collision between the pendulum and the pulley.
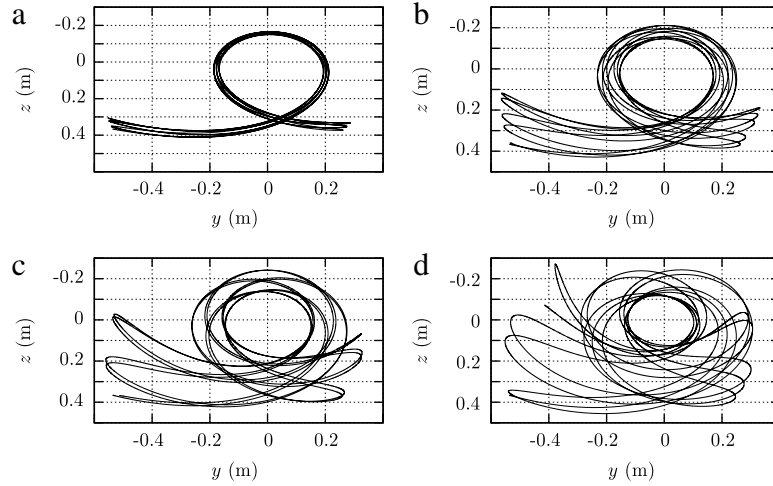
Fig. 12. Theoretical trajectories of the pendulum with pulleys of radius $R = 2.5$ cm and different moments of inertia I_p for $\mu_{exp} = 2.966$ and initial condition $(r_0; \theta_0) = (0.649 \text{ m}; 53.5°)$. (a) $I_p = 0$; this subplot which is the same as Fig. 11(b) has been repeated for the sake of clarity, (b) $I_p = 6.85 \times 10^{-6}$ kg m^2, (c) $I_p = 13.70 \times 10^{-6}$ kg m^2 and (d) $I_p = 27.40 \times 10^{-6}$ kg m^2.
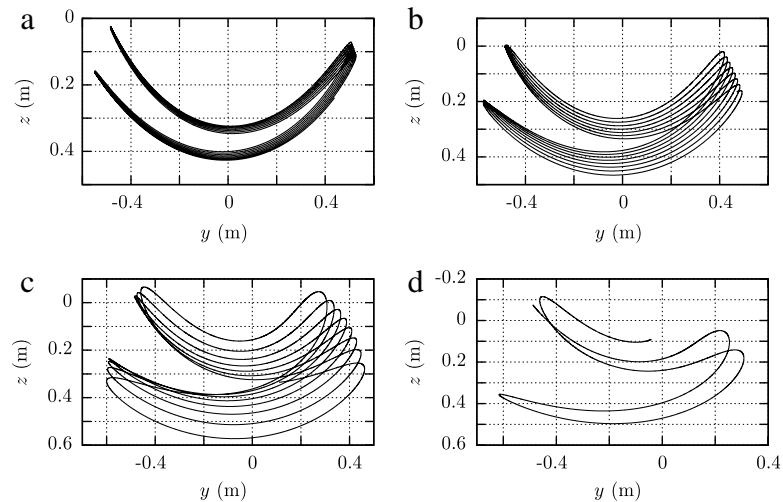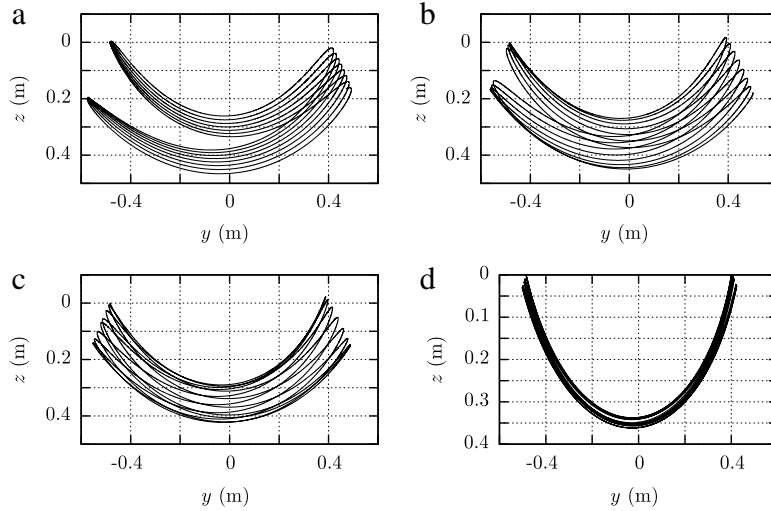

Fig. 13. Theoretical trajectories of the pendulum with fixed pulleys of different radii R for $\mu_{exp} = 1.525$ and initial condition $(r_0; \theta_0) = (0.484 \text{ m}; 87.0°)$. (a) $R = 0$, (b) $R = 2.5$ cm, (c) $R = 5$ cm and (d) $R = 10$ cm.
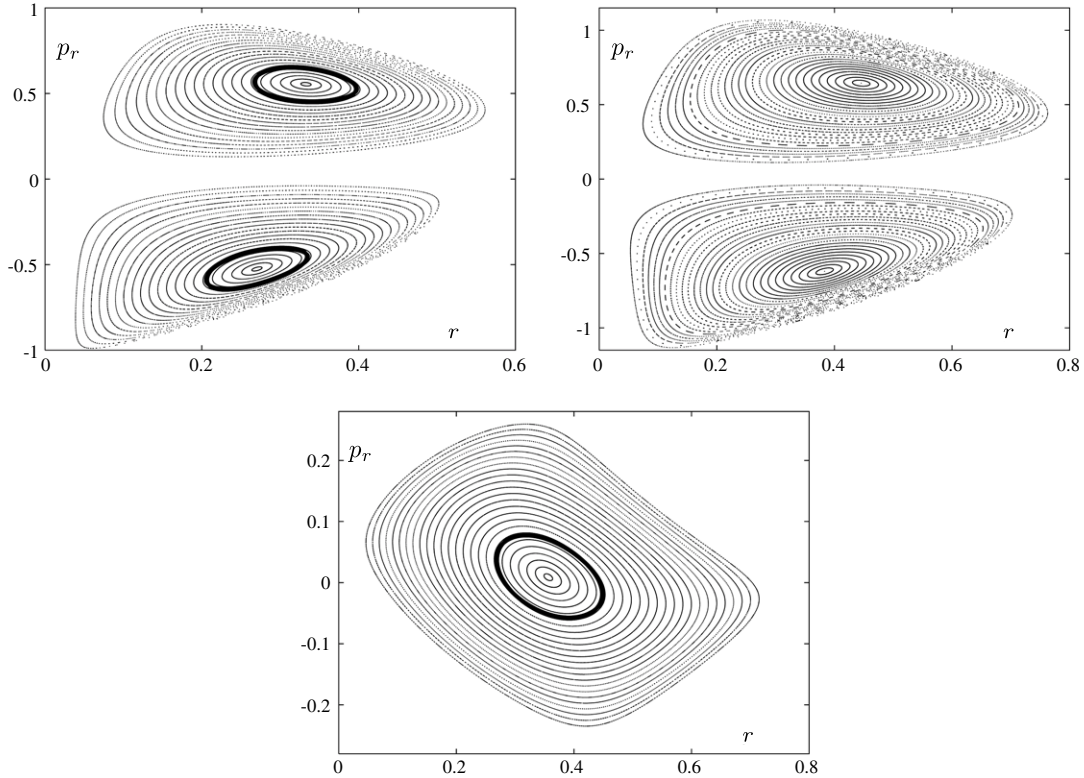
Fig. 14. Theoretical trajectories of the pendulum with pulleys of radius $R = 2.5$ cm and different moments of inertia I_p for $\mu_{\exp} = 1.525$ and initial condition $(r_0; \theta_0) = (0.484 \text{ m}; 87.0°)$. (a) $I_p = 0$; this subplot which is the same as Fig. 13(b) has been repeated for the sake of clarity, (b) $I_p = 6.85 \times 10^{-6}$ kg m^2, (c) $I_p = 13.70 \times 10^{-6}$ kg m^2 and (d) $I_p = 54.80 \times 10^{-6}$ kg m^2.


Fig. 15. Iterates of Poincaré maps for $M = 350$ g (top row) and $M = 180$ g (bottom plot) on the levels of energy of the physical experiments described in the text. The variables $(r; p_r)$, as usual in m and kg m s^{-1}, respectively, are shown for $\theta = 0 \pmod{2\pi}$ and $\dot{\theta} > 0$. On the top left plot, the points leave the section with $p_r > 0$ and $\theta = 0$, and those with $p_r < 0$ are in $\theta = -2\pi$. On the right top row, top initial points are in $\theta = 0$ with $p_r < 0$, and those showing in $p_r > 0$ have $\theta = 2\pi$. On the bottom plot, all intersections occur at $\theta = 0$. The thick curves are the intersections of the theoretical 2D tori corresponding to the physical experiments with the section Σ.

The bottom plot corresponds to $M = 180$ g. In that case, only intersections having $\theta = 0$ are found. The fixed point is $(r^*; p_r^*) \approx (0.356386 \text{ m}; 0.008848 \text{ kg m s}^{-1})$, which can also be obtained leaving from $(r_0; \theta_0) = (0.53313 \text{ m}; 78.596°)$, again not too far from the values used in the experiment. As before, the curve drawn with large points around the periodic orbit would be the one obtained for the physical experiment without dissipation and, as expected, denotes motion on a 2D torus.

A useful tool to understand the dynamics of Area-Preserving Maps and, in particular, Poincaré maps such as the ones displayed,

is the *rotation number* ρ for the map restricted to invariant curves. Despite the fact that the rotation number still exists for periodic orbits of $\mathcal{P}_m$ and for the eventual islands around them (thereupon being rational), it is not defined, in general, for orbits with chaotic dynamics. The method used for the computation is topological and based on the order of the arguments of the iterates with respect to the central fixed point $(r^*; p_r^*)$ of $\mathcal{P}_m$. The procedure computes two estimates $\rho_{\inf}$ and $\rho_{\sup}$ such that $\rho_{\inf} \leq \rho \leq \rho_{\sup}$. If for some orbit one has $\rho_{\inf} > \rho_{\sup}$ this proves ρ not defined. If the number of $\mathcal{P}_m$ iterates is N, the typical errors, when ρ exists, are $O(N^{-2})$
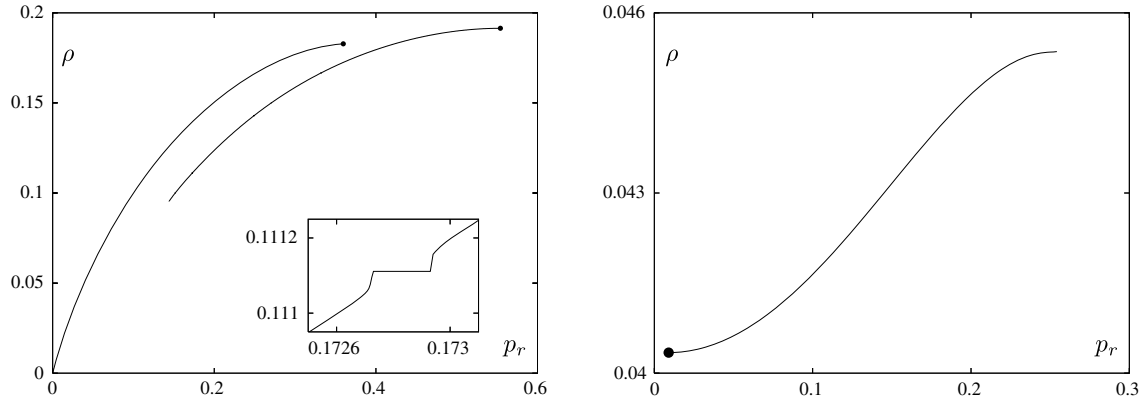
Fig. 16. Plots of rotation number for different cases. Left plot: the rotation number ρ as a function of the initial value of p_r with $r = r^*$ for $M = 350$ g and also for the pulley-less case with $\mu = 3$. A zoom-in around a resonance is shown in the inset. Right plot: ρ as a function of p_r for $M = 180$ g. See the text for additional details.

for constant type rotation numbers. See the Appendix in [19] for details and a complete analysis of the error depending on the diophantine properties of ρ.

In Fig. 16, we show results corresponding to the Poincaré maps displayed in Fig. 15 top and bottom. The computations are done starting at initial points of the form $(r^*; p_r)$ with $p_r = p_r^* - j\Delta$, $j = 1, 2, \ldots$ with a small step Δ. As successive iterates fall in Σ for values of θ alternating between 0 and -2π, the map $\mathcal{P}_m^2$ has been used instead of $\mathcal{P}_m$. On the left plot, we display ρ as a function of p_r for $M = 350$ g. This is the curve which has a large dot near the upper right corner. The point corresponds to $p_r = p_r^*$ and the limit rotation number. We see a decreasing rotation number when p_r decreases up to a value $p_r \approx 0.143982$ kg m s^{-1}. Beyond that point, the $\mathcal{P}_m$ iterates escape. The other curve, also shown here for comparison, corresponds to the pulley-less case with $\mu = 3$ and will be described later.

In fact, what seems a nice curve for $M = 350$ g should have, generically, a "devil's staircase" structure. That is, there are infinitely many intervals in which $\rho \in \mathbb{Q}$ and it is constant. They correspond to islands around elliptic fixed points. Some of these rational values, such as $1/6$, $1/7$, $1/9$, $3/20$, ... (or resonances) have been detected. But they are very narrow. As an example, the inset in the left plot of Fig. 16 shows the behaviour of ρ in an interval of p_r whose width is lower than 10^{-3} kg m s^{-1} and ρ around $1/9$, which illustrates a typical pattern when crossing a resonance through an island.

On the right-hand side of Fig. 16, we show the results for $M = 180$ g. As before, we use initial points $(r^*; p_r)$ with p_r going away from the fixed point of $\mathcal{P}_m$. $\mathcal{P}_m^2$ has also been used instead of $\mathcal{P}_m$ because the latter is close to a symmetry with respect to $(r^*; p_r^*)$, hence the displayed rotation number is small. It increases monotonously as we move away from the fixed point, also marked as a large dot. Now, however, the intervals with $\rho \in \mathbb{Q}$ constant are extremely narrow. We observed a few resonances, such as $2/45$ and $5/116$, checking that the width of p_r-intervals is below 10^{-6} kg m s^{-1}.

We want to mention now that the pattern of ρ as a function of p_r is a clear indication of non-integrability. Indeed, let us first look at the left plot in Fig. 16. We have also shown the results for *SAM* without pulleys and $\mu = 3$, the integrable case. The level of energy is the one corresponding to $(r_0; \theta_0) = (0.25$ m$; 0.0°)$, similar to the kind of reference orbits used in [12]. A periodic orbit is found near $(r^*; p_r^*) = (0.125$ m$, 0.369587$ kg m s$^{-1})$. Using $r = r^*$ and p_r between p_r^* and zero, we check that ρ decreases to zero. Under $\mathcal{P}_m^2$ there is a "separatrix" bounded by $r = 0$, $p_r = 0$ and a curve of the form $r = 0.25 - \alpha p_r^2$ for a suitable α. The system being integrable, the map $\mathcal{P}_m^2$ has a first integral I and the iterates are on level curves

of I. When approaching the separatrix, the dynamics slows down near $r = 0$ and p_r, hence ρ is very small.

But in the pulley case, the rotation number ceases to exist at a value which is unrelated to any separatrix. This is against the typical behaviour of integrable maps.

One should expect chaotic dynamic regions in a resonance zone in *SAM* with pulleys. Beyond the islands around periodic elliptic points, there are homoclinic tangles associated to the hyperbolic zones. Attempts to visualize them lead to the conclusion that the size of the "chaotic zones" is, at most, of the order of magnitude of the round-off errors with standard double precision computation. Hence, the escape remains a main evidence of non-integrability.

6.4. Remarks on dissipation

As we have already noted, experiments show non-negligible dissipative phenomena which decrease mechanical energy during the motion. Hence, equations of motion such as (4) which do not contain any dissipation term yield by no means a complete description of *SAM* dynamics.

In order to show that the observed convergence of the pendulum towards the pulley (Fig. 5(a)) is due to dissipation and not to a too short integration time interval, the corresponding theoretical trajectory (Fig. 10(a)) has been integrated for much larger intervals. Trajectories are not shown but we can say that the limited region of space occupied by the pendulum in Fig. 10(a) is progressively filled as time is running. The corresponding Tufillaro trajectory integrated for larger time is in addition symmetrical.

Four main different sources of dissipation can be noted: air friction on the pendulum and the counterweight, thread friction on the pulley grooves due to an imperfect absence of slippage condition, and dissipation due to the ball bearing of the pulleys. This last source is in part implicitly included in the equation of motion through the measure of I_p since it has been determined using a pulley (see Section 5.1).

An estimation of air friction can be performed by comparing the weight of the pendulum, mg, to the drag force exerted by air on the pendulum, whose expression is:

$$F_d = C_d \frac{\rho_a v^2}{2} S$$

where C_d is the drag factor, $\rho_a = 1.29$ kg m^{-3} the air density at ambient temperature $T = 298$ K, v the velocity of the ball, and S the effective surface of the pendulum. For a spherical ball, $C_d \approx 0.4$. Since $v \approx 1$ m s^{-1}, $S = \pi D_b^2/4$ with $D_b = 30$ mm, the drag-weight ratio is of the order of 2×10^{-4}. One gets the same order of magnitude for the cylindrical counterweight for which $C_d \approx 1$. Dissipation will be the detailed topic of a further paper.

7. Non-integrability of *SAM* with pulleys

In this section, a rigorous and original analytical proof of non-integrability of *SAM* is performed in order to complete the above rotation number and Poincaré section analysis. Needless to say, this non-integrability result is fundamentally different, both in approach and scope, from the numerical and graphical inference.

Since *SAM* may be expressed in terms of symplectic formalism, in order to detect or predict chaotic behaviour, it is pertinent to recall some concepts related to the integrability of Hamiltonian systems in the sense of Liouville–Arnold.

7.1. Algebraic background for studying integrability

7.1.1. Linear and Hamiltonian integrability

Differential Galois theory. See [20–22] for more information. Given a *linear* differential system, with coefficients in a differential field (K, ∂) whose field of constants $\mathcal{C}$ is algebraically closed (e.g. $[\mathbb{C}(t), \, \mathrm{d}/\mathrm{d}t]$),

$$\partial \boldsymbol{y} = A(t)\, \boldsymbol{y}, \tag{8}$$

an algebraic group G exists, called the *differential Galois group* of (8), acting over the $\mathbb{C}$-vector space $\langle \boldsymbol{\psi}_1, \ldots, \boldsymbol{\psi}_n \rangle$ of solutions of (8) as a linear transformation group over $\mathbb{C}$. Furthermore, G contains the monodromy group of (8). The Galoisian formalism proves useful here due to the following: (8) *is integrable (i.e. its general solution can be written as a finite sequence of quadratures, exponentials, and algebraic functions) if, and only if, the identity component G^0 of the differential Galois group G of* (8) *is solvable.*

Everything said in the previous paragraph may be obtained, *mutatis mutandis*, for linear homogeneous differential equations

$$a_n(t)\frac{\mathrm{d}^n}{\mathrm{d}t^n}y + a_{n-1}(t)\frac{\mathrm{d}^{n-1}}{\mathrm{d}t^{n-1}}y + \cdots + a_1(t)\frac{\mathrm{d}}{\mathrm{d}t}y + a_0(t)\,y = 0.$$

In Section 7.1.3, we will denote Galois groups in this $\mathrm{Gal}(L)$ accordingly, $L \in \mathbb{C}(t)[\mathrm{d}/\mathrm{d}t]$ being the corresponding differential operator. See [23] for more details.

Liouville–Arnold integrability. On the other hand, we call a Hamiltonian system $\dot{\boldsymbol{q}} = \partial\mathcal{H}/\partial\boldsymbol{p}, \dot{\boldsymbol{p}} = -\partial\mathcal{H}/\partial\boldsymbol{q}$, whether or not linear, *meromorphically integrable (in the sense of Liouville–Arnold)*, if it has as many independent meromorphic first integrals in pairwise involution as degrees of freedom. Same applies in the above definition, *mutatis mutandis*, substituting *algebraic*, *rational* or any other function class in for *meromorphic*. For the sake of simplicity, conjugate canonical variables will be henceforth assembled in a single vector $\boldsymbol{z} = (\boldsymbol{q}, \boldsymbol{p})$ and the Hamiltonian system will be written in compact form $\dot{\boldsymbol{z}} = X_{\mathcal{H}}(\boldsymbol{z})$. *Everything is considered in the complex analytical setting from this point on.*

7.1.2. Morales–Ramis–Ziglin theory

For each integral curve $\Gamma = \left\{ \tilde{\boldsymbol{\phi}}(t) : t \in I \right\}$ of a given autonomous dynamic system in dimension m

$$\dot{\boldsymbol{z}} = X(\boldsymbol{z}), \tag{9}$$

the *variational equations* of order k for (9) along Γ, VE_Γ^k, are satisfied by $\Xi_k := \partial^k \tilde{\boldsymbol{\phi}}/\partial \boldsymbol{z}^k$ — see, e.g., [24] for explicit expressions of VE_Γ^k for general k in terms of vectors $\boldsymbol{k} = (k_1, \ldots, k_m) \in \mathbb{Z}_+^m$ such that $k = k_1 + \cdots + k_m$. Note that $\partial^k \tilde{\boldsymbol{\phi}}/\partial \boldsymbol{z}^k$ is an abridged notation for the $(k+1)$-dimensional matrix of all partial derivatives of $\tilde{\boldsymbol{\phi}}$. In other words, it is a vector for $k = 0$, a matrix for $k = 1$, etc.

In particular, for $k = 1$ and denoting the matrix of the first-order variational equations simply by Ξ, we obtain

$$\dot{\Xi} = X'\left(\tilde{\boldsymbol{\phi}}\right)\Xi. \tag{VE$_\Gamma$}$$

We thus have:

- a *(generally nonlinear)* system (9) and
- a *linear system* (VE_Γ) linked to (9).

The hallmark theorem in this approach connects the two notions of solvability listed in 7.1.1, namely as applied to a Hamiltonian $X_{\mathcal{H}}$ and its variational equations (VE_Γ), along an integral curve Γ of $X_{\mathcal{H}}$. The whole theory is actually the *ad hoc* implementation of the following heuristic principle: if a Hamiltonian is integrable, then its variational equations must also be integrable.

We assume Γ, a Riemann surface, may be locally parameterized in a disc $I \subset \mathbb{C}$ of the complex plane; we may now complete Γ to a new Riemann surface $\overline{\Gamma}$, as detailed in [25, Section 2.1] (see also [20, Section 2.3]), by adding equilibrium points, singularities of the vector field and possibly $t = \infty$.

Theorem 7.1 (*[25]*). *Let $\mathcal{H}$ be an n-degree-of-freedom Hamiltonian having n independent first integrals in pairwise involution, defined on a neighbourhood of an integral curve $\overline{\Gamma}$. Then, the identity component* $\mathrm{Gal}\left(\mathrm{VE}_{\overline{\Gamma}}\right)^0$ *is an abelian group (i.e. $\mathrm{Gal}\left(\mathrm{VE}_{\overline{\Gamma}}\right)$ is virtually abelian).*

See [25, Corollary 8] or [20, Theorem 4.1] for a precise statement and a proof.

7.1.3. Differential operators: A primer in the Boucher–Weil Theorem

Linear differential equations. See [26, Section 2] for more details. Let

$$L = a_n\left(\frac{\mathrm{d}}{\mathrm{d}t}\right)^n + a_{n-1}\left(\frac{\mathrm{d}}{\mathrm{d}t}\right)^{n-1} + \cdots + a_0; \quad a_n, \ldots, a_0 \in \mathbb{C}(t)$$

be a differential operator with coefficients in the field of formal Laurent series. If $L(y) = 0$ has a solution of the form $y = t^\rho \sum_{k\geq 0} c_k t^k$ and $c_0 \neq 0$, the formal substitution of y into the differential equation yields the vanishing of all powers of t, the smallest one among them — we call the equation $P(\rho) = 0$ derived from the latter vanishing the *indicial equation* (at 0), the roots of which are usually called *exponents* of $L(y)$ (at 0). In particular we can also define the indicial equation at infinity by means of the transformation $f = 1/t$ and expansion around $f = 0$.

It is a known fact [26, Lemma 2.1] that the degree of $P(\rho) = 0$ is at most n. A singular point c of L is called *regular singular* if $\deg P(\rho) = n$. A linear differential equation $L = 0$ with only regular singular points (including ∞) is called *Fuchsian*.

We call L *reducible* if it factors in a product of operators of smaller positive order. An operator L admits a first-order factor $\mathrm{d}/\mathrm{d}t - f, f \in \mathbb{C}(t)$ if and only if $L(y) = 0$ admits a solution y such that $\dot{y} = fy$; in particular:

Lemma 7.2. *If L is of order 2: L is reducible if, and only if, it has an exponential solution, i.e. a solution whose logarithmic derivative is rational.* □

Lemma 7.3 (*[26, Section 3.1.2]*). *If L is Fuchsian, every exponential solution must be of the form $\tilde{y} = \prod_{i=1}^{s}(t - t_i)^{e_i}P(t)$, where $P \in \mathcal{C}[X]$ and $t_1, \ldots, t_s$ are finite singularities of L with exponents $e_1, \ldots, e_s$, whether or not integers.*

Normal variational equations. Let

$$J = \begin{pmatrix} 0 & \mathrm{Id}_n \\ -\mathrm{Id}_n & 0 \end{pmatrix}$$

be the canonical symplectic matrix. Given a Hamiltonian system $\dot{\boldsymbol{z}} = X_{\mathcal{H}}(\boldsymbol{z}) = J\nabla\mathcal{H}(\boldsymbol{z})$ expressed in Darboux canonical coordinates $\boldsymbol{z} = (\boldsymbol{q}, \boldsymbol{p})$, system (VE_Γ) reads $\dot{\Xi} = J\mathcal{H}''(\tilde{\boldsymbol{z}})\,\Xi$ along $\Gamma = \left\{\tilde{\boldsymbol{z}}(t)\right\}$.

Gauge transformations. $A \mapsto P[A] := P^{-1}\left(AP - \dot{P}\right), P$ being a given symplectic matrix, may be used to reduce (VE_Γ) by selectively vanishing a number of entries in $J\mathcal{H}''(\tilde{\boldsymbol{z}})$ (see

[27, Section 5.2], [20, Section 4.1], [28]). A typical first choice consists of symplectic matrices of the form

$$P(t) = \left(\frac{\mathrm{d}}{\mathrm{d}t}\tilde{z} \quad c_2 \quad c_3 \quad c_4 \right), \tag{10}$$

in order to induce a row and a column of zeroes in the variational matrix. When such is the case, (VE$_\Gamma$) acquires a "decoupled" appearance and a system of order $n-2$ may be extracted therefrom. Such a system is usually called a *normal variational system* along Γ. Let us denote it by NVE$_\Gamma$.

As is always the case with all differential systems, a *cyclic vector* [27,29] may be used to obtain a linear differential equation $L(y) = 0$ of order $n-2$ equivalent to NVE$_\Gamma$.

The result central to this paragraph, and a particularly useful consequence of Theorem 7.1, is the following (see also [27, Proposition 9 & Theorem 8 (Section 5.3)]).

Theorem 7.4 ([30, Criterion 1]). *Let $X_{\mathcal{H}}$ be a Hamiltonian system and L its normal variational operator along a given particular solution. If L is irreducible and displays logarithms in a formal solution, then* Gal$(L)^0$ *is not abelian, i.e. $X_{\mathcal{H}}$ is not integrable.* □

Typically, the most difficult part in trying to apply Theorem 7.4 is to check the irreducibility condition.

7.2. Statement of the main result

We recall $M_t = M + m + 2I_p/R^2$ and

$$\mathcal{H} = \frac{1}{2}\left[\frac{p_1^2}{M_t} + \frac{(p_2 + Rp_1)^2}{mq_1^2} \right] + gq_1(M - m\cos q_2) - gR(Mq_2 - m\sin q_2),$$

where $q_1 = r$, $q_2 = \theta$, $p_1 = p_r$, and $p_2 = p_\theta$. The main result in this Section is the following.

Theorem 7.5 (*Non-Integrability of SAM with Massive Pulleys*). *For every physically consistent value of the parameters, regardless of I_p and R, $X_{\mathcal{H}}$ is meromorphically non-integrable.*

This is a complement to what has already been proved for *SAM without pulleys*, i.e. the limit case $I_p = 0$, $R = 0$ and $M_t = M + m$:

$$\mathcal{H}_w = \frac{1}{2}\left(\frac{p_1^2}{M_t} + \frac{p_2^2}{mq_1^2} \right) + gq_1(M - m\cos q_2); \tag{11}$$

in that case, the following held.

Theorem 7.6 (*SAM Without Massive Pulleys*).

1. ([7, Theorem 1], [8, Eq. (16)], [9]; see also Remark 7.1 (2)) If $M > m$ and

$$\mu = \frac{M}{m} \neq \mu_p := \frac{p(p+1)}{p(p+1) - 4}$$

for every $p \in \mathbb{Z}$, $p \geq 2$, then Hamiltonian $X_{\mathcal{H}_w}$ is non-integrable. In particular, if $\mu \in (3/2, 3) \cup (3, \infty)$, it is non-integrable.
2. [5, Eq. (16)] For $p = 2$, $\mu = \mu_2 = 3$, $X_{\mathcal{H}_w}$ is integrable and has the following first integral:

$$I = q_1^2\dot{q}_2\left(\dot{q}_1 c - \frac{q_1\dot{q}_2}{2}s \right) + gq_1^2 sc^2$$

$$= gq_1^2 c^2 s + p_2\frac{p_1 q_1 c - 2p_2 s}{4m^2 q_1},$$

where $c = \cos(q_2/2)$, $s = \sin(q_2/2)$.
3. [12, Theorem 4] The degenerate cases μ_p, $p \geq 2$ referred to in item 1 are non-integrable. □

The last case is significantly more difficult; it relies on the higher-order variational equations [24] and uses techniques introduced in [31].

7.3. Proof of Theorem 7.5

We have two particular solutions for *SAM* with massive pulleys:

$$\boldsymbol{z}_{0,R}(t) = \frac{g(M-m)}{2}\left(\frac{t(1-t)}{M_t}, 0, 1 - 2t, R(2t - 1) \right),$$

$$\boldsymbol{z}_{\pi,R}(t) = \frac{g(M+m)}{2}\left(\frac{t(1-t)}{M_t}, \frac{2\pi}{g(M+m)}, 1 - 2t, R(2t - 1) \right).$$

System (VE$_\Gamma$) around $\Gamma = \{\boldsymbol{z}_{\pi,R}(t)\}$ takes the form $\dot{\Xi} = A\Xi$ with

$$A = \begin{pmatrix} 0 & 0 & 1/M_t + R^2 a_1 & Ra_1 \\ 0 & 0 & Ra_1 & a_1 \\ 0 & 0 & 0 & 0 \\ 0 & a_2 & 0 & 0 \end{pmatrix},$$

where

$$a_1 = \frac{4M_t^2}{mg^2(M+m)^2 t^2(t-1)^2} \quad \text{and}$$

$$a_2 = -\frac{mg^2(M+m)t(t-1)}{2M_t}.$$

Notably, (VE$_\Gamma$) decouples without the need for an additional gauge transformation such as (10) as is usual and customary [27,30,20], and as would be the case if $\Gamma = \{\boldsymbol{z}_{\pi,0}(t)\}$. See Remark 7.1 1 below. System NVE$_\Gamma$ takes the form $\dot{\Phi} = B\Phi$ with

$$B = \begin{pmatrix} 0 & a_1 \\ a_2 & 0 \end{pmatrix}.$$

A necessary condition of integrability is the virtual abelianity (see Theorem 7.1) of Gal (NVE$_\Gamma$) , NVE$_\Gamma$, by means of a *cyclic vector* $\boldsymbol{c}$ and the subsequent gauge transformation given by $\Phi = Q^{-1}\tilde{\Phi}$, where $Q = \left(\boldsymbol{c} \quad \dot{\boldsymbol{c}} + B^T\boldsymbol{c} \right)^T$ [27, Section B.4], will take the form

$$\frac{\mathrm{d}}{\mathrm{d}t}\tilde{\Phi} = \begin{pmatrix} 0 & 1 \\ -\dfrac{2M_t}{(M+m)(t-1)t} & -\dfrac{2(2t-1)}{(t-1)t} \end{pmatrix}\tilde{\Phi},$$

in presence of a constant cyclic vector $\boldsymbol{c} = (a, 0)$. The above system is obviously equivalent to the following *hypergeometric* [32, Section 15.5], hence Fuchsian differential operator:

$$L = \left(\frac{\mathrm{d}}{\mathrm{d}t} \right)^2 + \frac{2(2t-1)}{t(t-1)}\frac{\mathrm{d}}{\mathrm{d}t} + \frac{2M_t}{(M+m)t(t-1)}.$$

Let us now check the virtual non-commutativity of Gal (L). L has three singularities: 0, 1, ∞. At $t = 0$ or $t = 1$, we have local exponents -1 and 0. The formal solution at $t = 0$ has logarithms except in two cases: $m = 0$, $M_t = M + m$, both discarded in our case since they would correspond to no small mass and no pulley, respectively. Indeed, a particular solution is

$$\tilde{y}_1(t) = {}_2F_1\left(\frac{3}{2} - \frac{[9(M+m) - 8M_t]^{1/2}}{2(M+m)^{1/2}}, \frac{3}{2} \right.$$

$$\left. + \frac{[9(M+m) - 8M_t]^{1/2}}{2(M+m)^{1/2}}; 2; t \right),$$

where

$${}_2F_1(a, b; c; t) = \sum_{k=0}^{\infty} \frac{(a)_k(b)_k}{(c)_k}\frac{t^k}{k!}$$

is the *Gauss hypergeometric function* [32, Section 15.1], $(a)_k = a(a+1)\cdots(a + k - 1)$ being the *Pochhammer symbol*. This first solution has a local expansion around $t = 0$ of the form

$$\tilde{y}_1 = 1 + \frac{M_t}{M+m}t + \frac{M_t[2(M+m) + M_t]}{3(M+m)^2}t^2 + O(t^3).$$

We may then obtain an expansion for a second formal solution

$$\tilde{y}_2 = -\frac{1}{t} - \frac{M_t}{M+m} + \left\{ 3 + \frac{2M_t \left[M_t - 3(M+m) \right]}{(M+m)^2} \right\} t$$
$$+ O\left(t^2\right) + 2 \frac{M+m-M_t}{M+m} \tilde{y}_1 \ln t.$$

Keeping the Boucher–Weil Theorem 7.4 in mind, and in presence of the logarithm in $\tilde{y}_2$, there is obstruction to integrability if L is irreducible.

Let us assume it is reducible. In virtue of Lemma 7.2, L admits an exponential solution. We recall that L is Fuchsian. The expansion of an exponential solution around $t = 0$ does not contain logarithms, although we have shown there are formal solutions with logarithms around the singularities − as has been seen explicitly for $t = 0$. Thus, those without logarithms correspond to the maximal exponents [33], hence the admissible exponents at the finite singularities are all 0. Hence, in virtue of Lemma 7.3, the only possible form for an exponential solution $\tilde{y}$ would be that of a polynomial solution; let N be its degree. Expanding $\tilde{y}$ in increasing powers of t^{-1}, $-N$ is the exponent of the leading term, hence an exponent at infinity: $\sum_{k=0}^{N} a_k t^k = (1/t)^{-N} \sum_{k=0}^{N} a_{N-k} (1/t)^k$.

Now, the exponents at infinity are the two roots of the indicial equation $\rho^2 - 3\rho + 2M_t/(M+m)$. Since $-N$ is such a root, this means $M_t = -N(N+3)(M+m)/2$ with N positive. Therefore M_t would be negative, which is physically irrelevant.

Hence follows that the Swinging Atwood Machine system with massive pulleys is *always* non-integrable with meromorphic first integrals. □

Remark 7.1. 1. Intriguingly, the solution used for our proof was $\boldsymbol{z}_{\pi,R}$, which, at least for the pulley-less case $R \to 0, M_t \to M + m$, and although mathematically plausible, has no actual physical significance. The solution which would be physically possible for all values of R, $\boldsymbol{z}_{0,R}$, posed further problems with regards to system (VE_Γ) and was finally discarded in our proof. It is worth mentioning, however, that in the case without pulleys, [12] used precisely the corresponding form of the latter solution $\boldsymbol{z}_{0,0}$.

2. The same proof given for Theorem 7.5 may be obtained, analogously, for *SAM* without pulleys $\mathcal{H}_w, \mu > 1$, and the proof yields precisely item 1 in Theorem 7.6. Indeed, by using the "classical" solution $\boldsymbol{z}_{0,0}$ (which corresponds to the original Atwood machine) and an adequate gauge transformation, we obtain the normal variational equation:

$$-\frac{2M_t}{(M-m)t(t-1)} y(t) - \frac{(2t-1)}{(t-1)t} \frac{\mathrm{d}}{\mathrm{d}t} y(t) + \frac{\mathrm{d}^2}{\mathrm{d}t^2} y(t) = 0.$$

This is a Gauss hypergeometric equation. Local solutions are

$$t^2 - \frac{2}{3} \left(\frac{M_t}{M-m} + 1 \right) t^3 + O\left(t^4\right),$$

and

$$-\frac{(M-m)\left[2t M_t + (M-m)\right]}{2M_t \left[M_t + (M-m)\right]} + O\left(t^2\right)$$
$$+ \left[t^2 - \frac{2}{3} \left(\frac{M_t}{M-m} + 1 \right) t^3 + O\left(t^4\right) \right] \ln t.$$

The degenerate cases $M_t = 0$ and $M_t + M - m = 0$ are of course not physically acceptable. The exponents at zero are 0 and 2, the exponents at $t = 1$ are also 0 and 2, and the exponents at infinity are the roots of the polynomial $P_\infty(X)$ where $P_\infty(X) = (M-m)X^2 + 3(M-m)X - 2M_t$. Same as in the proof of Theorem 7.5, reducibility would occur only for a

polynomial solution, i.e. in presence of an integer N such that $P_\infty(N) = 0$, implying

$$M_t = \frac{1}{2}(N+4)(N+1)(M-m).$$

Setting $M_t = M + m$ (that is, the pulley-less case) we would have an equation for μ whose solution would be

$$\mu = \frac{N^2 + 5N + 6}{N^2 + 5N + 2} = \frac{(N+3)(N+2)}{(N+3)(N+2) - 4},$$

obviously equivalent to the condition in item 1 in Theorem 7.6 for $N = p - 2$.

3. For $\mu = 1$, however, the closest thing to such a proof as that sketched in item 2 is discarding the existence of first integrals with a meromorphic growth at infinity, e.g. rational ones. This is due to the fact that the normal variational equation around particular solution $\tilde{\boldsymbol{z}}(t) = (-gt/2; 0; -gm; 0)$ is a *Hamburger equation*,

$$-\frac{2}{t} y(t) - \frac{1}{t} \frac{\mathrm{d}}{\mathrm{d}t} y(t) + \frac{\mathrm{d}^2}{\mathrm{d}t^2} y(t) = 0,$$

i.e. an equation with exactly two singularities: a regular one at zero and an irregular one at infinity [34, Section 17.6]; the solutions are almost Bessel functions: the general solution is:

$$y(t) = C_1 t I_2\left(2\sqrt{2t}\right) + C_2 t K_2\left(2\sqrt{2t}\right), \quad C_1, C_2 \in \mathbb{C},$$

where, $n \in \mathbb{Z}$ given, $I_n(z)$ and $K_n(z)$ are the *modified Bessel functions of the first and second kind*, respectively [35, p. 416], [32, p. 376], [36, p. 185]:

$$I_n(z) = \frac{1}{2\pi i} \int_{\mathbb{S}^1} \frac{\exp\left[(z/2)(t+1/t)\right]}{t^{n+1}} \, \mathrm{d}t,$$
$$K_n(z) = \frac{\pi}{2} \frac{I_{-n}(z) - I_n(z)}{\sin(n\pi)},$$

both having a branch cut discontinuity in the complex z plane running from $-\infty$ to 0 (although I_n is regular at 0, whereas K_n has a logarithmic divergence at 0). This assures the presence of a non-trivial Stokes multiplier at infinity for the variational equation when $\mu = 1$. This implies the following important conclusion: *the system is not integrable with first integrals which are rational functions of r, θ, $\cos\theta$, $\sin\theta$, p_r, p_θ, where θ belongs to a neighbourhood of 0.*

Indeed, any first integral is a function of $(\boldsymbol{q}, \boldsymbol{p})$, hence must be defined on the phase manifold $M := \mathbb{C}^4$. We can partially compactify M into $\tilde{M} := \mathbb{P}^2_\mathbb{C} \times \mathbb{C}^2$, where $\mathbb{P}^2_\mathbb{C}$ stands for the compactification, by means of the inverse stereographic projection P^{-1}, of the domain $\mathbb{C}^2$ for $(q_1; p_1) = (r; p_r)$, whereas the second factor $\mathbb{C}^2$ is the $(\theta; p_\theta)$-plane. Using $P^{-1}|_{\overline{\Gamma}}$ in order to compactify the particular solution $\overline{\Gamma} = \{\tilde{\boldsymbol{z}}(t)\}$, we obtain a Riemann sphere $\tilde{\Gamma}$ in $\mathbb{P}^2_\mathbb{C}$, whose immersion in $\mathbb{P}^2_\mathbb{C} \times \mathbb{C}^2$ is contained in $\{\theta = 0\}$; therefore $\cos\theta$, $\sin\theta$ are holomorphic, hence meromorphic on a neighbourhood of $\tilde{\Gamma}$ in $\tilde{M}$. Theorem 7.1 implies the absence of a complete set of first integrals which are meromorphic on a neighbourhood of $\tilde{\Gamma}$ in the partial compactification $\tilde{M}$. Since any rational function of r, θ, p_r, p_θ, $\cos\theta$, $\sin\theta$ must be meromorphic in a neighbourhood of $\tilde{\Gamma}$ in $\tilde{M}$, we obtain the last claim in the previous paragraph.

8. Conclusion and perspectives

In this paper, experimental and theoretical results concerning the *Swinging Atwood Machine* are presented. Equations of motion with two pulleys are found generalizing those of previous studies. An experimental device for *SAM* is constructed and described in

detail. Experiments are conducted and the trajectories retrieved from computer video analysis closely match those arising from numerical solution of the equations of motion. Such comparisons seem to show that the motion is influenced by the non-negligible dimension and the rotation of the pulleys; in particular, a non-zero pulley radius leads to asymmetric pendulum trajectories. We conclude that pulleys cannot be ignored in *SAM* dynamics.

Finally, after giving some numerical evidence of the lack of integrability of *SAM* in the absence of dissipation, a complete proof of this fact is given using differential Galois theory and the necessary conditions following from Morales–Ramis theory.

Several perspectives of this work can be considered. First of all, other experiments are currently conducted with $\mu_{exp} = 2.03$ and qualitative preliminary results (not shown in this paper) indicate that the dynamics of *SAM* seems to be irregular — chaotic behaviour is expected. Detailed research will be performed in a future work. Secondly, the influence of dissipative phenomena on *SAM* dynamics should be studied; a possible procedure in such direction is increasing air friction by coating the pendulum with different materials, judiciously chosen so as to induce changes in drag force. Another method could consist in placing the counterweight in media more viscous than air, such as water or glycerin, and forcing it to evolve therein. Perhaps an ultrafast camera of about 1000 images per second could be necessary to pick up much more points and achieve a better resolution in pendulum trajectories. Also, a sensor to measure string tension during motion and analyze its evolution would be useful.

Concerning the integrability of *SAM* without pulleys, that is Hamiltonian $\mathcal{H}_w$ in (11) obtained from (5) by skipping the contributions of R and I_p, the results summarized in Theorem 7.6, along with the result shown in the previous section for $\mu = 1$, close the problem: the pulley-less case is non-integrable for all values of $\mu \neq 3$.

Acknowledgements

References

[1] G. Atwood, A Treatise on the Rectilinear Motion and Rotation of Bodies, Cambridge University Press, 1784.

[2] N.B. Tufillaro, T.A. Abbott, D.J. Griffiths, Swinging Atwood's machine, Amer. J. Phys. 52 (1984) 895–903.

[3] N.B. Tufillaro, Teardrop and heart orbits of a swinging Atwood's machine, Amer. J. Phys. 62 (1994) 231–233.

[4] N.B. Tufillaro, Motions of a swinging Atwood's machine, J. Physique 46 (1985) 1495–1500.

[5] N.B. Tufillaro, Integrable motion of a swinging Atwood's machine, Amer. J. Phys. 54 (1986) 142–143.

[6] I.C. Moreira, M.A. Almeida, Noether symmetries and the swinging Atwood machine, J. Physique II 1 (7) (1991) 711–715.

[7] J. Casasayas, A. Nunes, N.B. Tufillaro, Swinging Atwood's machine: integrability and dynamics, J. Physique 51 (1990) 1693–1702.

[8] H.M. Yehia, On the integrability of the motion of a heavy particle on a tilted cone and the swinging Atwood's machine, Mech. Res. Comm. 33 (5) (2006) 711–716.

[9] M.A. Almeida, I.C. Moreira, F.C. Santos, On the Ziglin–Yoshida analysis for some classes of homogeneous Hamiltonian systems, Preprint.

[10] N.B. Tufillaro, A. Nunes, J. Casasayas, Unbounded orbits of a swinging Atwood's machine, Amer. J. Phys. 56 (1988) 1117–1120.

[11] A. Nunes, J. Casasayas, N.B. Tufillaro, Periodic orbits of the integrable swinging Atwood's machine, Amer. J. Phys. 63 (1995) 121–126.

[12] R. Martínez, C. Simó, Non-integrability of the degenerate cases of the swinging Atwood's machine using higher order variational equations, 2009 (under revision process).

[13] G.D. Birkhoff, Dynamical Systems, American Mathematical Society, 1927.

[14] J.J. Morales-Ruiz, C. Simó, Non-integrability criteria for Hamiltonians in the case of Lamé normal variational equations, J. Differential Equations 129 (1996) 111–135.

[15] J.P. Pérez, Mécanique, fondements et applications, 6th ed., Dunod, Paris, 2001.

[16] O. Pujol, J.-P. Pérez, A simple formulation of the golf ball paradox, European J. Phys. 28 (2007) 379–384.

[17] H. Moritz, Geodetic reference system, Bull. Geod. 62 (1988) 348–358.

[18] C. Simó, Taylor method for the integration of ODE, Lectures given at the LTI07 Advanced Course on Long Time Integration, 2007. Available at: http://www.maia.ub.es/dsg/2007/.

[19] J. Sánchez, M. Net, C. Simó, Computation of invariant tori by Newton–Krylov methods in large-scale dissipative systems, Physica D 239 (2009) 123–133, doi:10.1016/j.physd.2009.10.012.

[20] J.J. Morales-Ruiz, Differential Galois Theory and Non-Integrability of Hamiltonian Systems, in: Progress in Mathematics, vol. 179, Birkhäuser Verlag, Basel, 1999.

[21] M. van der Put, M.F. Singer, Galois Theory of Linear Differential Equations, in: Grundlehren der Mathematischen Wissenschaften [Fundamental Principles of Mathematical Sciences], vol. 328, Springer-Verlag, Berlin, 2003.

[22] J.E. Humphreys, Linear Algebraic Groups, in: Graduate Texts in Mathematics, vol. 21, Springer-Verlag, New York, 1975.

[23] A.R. Magid, Lectures on Differential Galois Theory, in: University Lecture Series, vol. 7, American Mathematical Society, Providence, RI, 1994.

[24] J.J. Morales-Ruiz, J.-P. Ramis, C. Simó, Integrability of Hamiltonian systems and differential Galois groups of higher variational equations, Ann. Sci. Éc. Norm. Supér Sér. 4 40 (2007) 845–884.

[25] J.J. Morales-Ruiz, J.-P. Ramis, Galoisian obstructions to integrability of Hamiltonian systems. I, Methods Appl. Anal. 8 (1) (2001) 33–96.

[26] M.F. Singer, F. Ulmer, Necessary conditions for Liouvillian solutions of (third order) linear differential equations, Appl. Algebra Engrg. Comm. Comput. 6 (1) (1995) 1–22.

[27] D. Boucher, Sur les équations différentielles linéaires paramétrées; une application aux systèmes hamiltoniens, Ph.D. Thesis, Université de Limoges, 2000.

[28] A. Aparicio, J.-A. Weil, A reduced form for Hamiltonian systems with two degrees of freedom, Preprint, 2008.

[29] M.F. Singer, Direct and inverse problems in differential Galois theory, in: Selected Works of Ellis Kolchin with Commentary, American Mathematical Society, Providence, RI, 1999. Commentaries by Armand Borel, Michael F. Singer, Bruno Poizat, Alexandru Buium and Phyllis J. Cassidy, Edited and with a preface by Hyman Bass, Buium and Cassidy.

[30] D. Boucher, J.-A. Weil, Application of J J Morales and J-P Ramis' theorem to test the non-complete integrability of the planar three-body problem, in: From Combinatorics to Dynamical Systems, in: IRMA Lect. Math. Theor. Phys., vol. 3, de Gruyter, Berlin, 2003, pp. 163–177.

[31] R. Martínez, C. Simó, Non-integrability of Hamiltonian systems through high order variational equations: summary of results and examples, Regul. Chaotic Dyn. 14 (3) (2009) 323–348.

[32] M. Abramowitz, I.A. Stegun (Eds.), Handbook of Mathematical Functions with Formulas, Graphs, and Mathematical Tables, in: A Wiley-Interscience Publication, John Wiley & Sons Inc., New York, 1984. Reprint of the 1972 edition, Selected Government Publications.

[33] E.T. Whittaker, G.N. Watson, A Course of Modern Analysis, in: Cambridge Mathematical Library, Cambridge University Press, Cambridge, 1996. An introduction to the general theory of infinite processes and of analytic functions; with an account of the principal transcendental functions, Reprint of the fourth (1927) edition.

[34] E.L. Ince, Ordinary Differential Equations, Dover Publications, New York, 1944.

[35] G. Arfken, Modified Bessel functions, $I_\nu(x)$ and $K_\nu(x)$, in: Mathematical Methods for Physicists, 3rd ed., Academic Press, Orlando, FL, 1985 (Section 11.5).

[36] G.N. Watson, Treatise on the Theory of Bessel Functions, 2nd ed., Cambridge University Press, Cambridge, England, 1966.